NASA Technical Memorandum 104606, Vol. 16

Technical Report Series on
Global Modeling and Data Assimilation

Max J. Suarez, Editor
Goddard Space Flight Center
Greenbelt, Maryland

Volume 16

Filtering Techniques on a Stretched Grid General Circulation Model

Lawrence L. Takacs
William Sawyer
Max J. Suarez
Michael S. Fox-Rabinovitz

June 1999

Goddard Space Flight Center
Greenbelt, Maryland 20771

Abstract

This report documents the techniques used to filter quantities on a stretched grid general circulation model. Standard high-latitude filtering techniques (e.g. using an FFT to decompose and filter unstable harmonics at selected latitudes) applied on a stretched grid are shown to produce significant distortions of the prognostic state when used to control instabilities near the pole. A new filtering technique is developed which accurately accounts for the non-uniform grid by computing the eigenvectors and eigenfrequencies associated with the stretching. A filter function, constructed to selectively damp those modes whose associated eigenfrequencies exceed some critical value, is used to construct a set of grid-spaced weights which are shown to effectively filter without distortion. Both offline and GCM experiments are shown using the new filtering technique. Finally, a brief examination is also made on the impact of applying the Shapiro filter on the stretched grid.

Contents

List of Figures

1 Introduction

Version 2 of the Aries/GEOS dynamical core (Suarez and Takacs,1995) was developed at the Goddard Space Flight Center for use in data assimilation and climate prediction applications. In this paper we present a generalization of this dynamical core that allows for a non-uniform latitude/longitude ($\Delta\phi_j$, $\Delta\lambda_i$) grid. This capability allows use of the model for regional data assimilation with the Goddard Earth Observing System (GEOS) Data Assimilation System (DAS) (see Rood, 1996) and for regional prediction studies using the NASA Seasonal to Interannual Prediction Project's (NSIPP) coupled prediction system. The use of this dynamical core in conjunction with a non-uniform grid has been demonstrated by Fox-Rabinovitz et al. (1997) for the Held-Suarez (1994) dynamics benchmark. That work demonstrated the usefulness of achieving high resolution results over selected regions with much greater efficiency than employing high-resolution uniformly over the sphere.

The Aries/GEOS dynamical core relies on two filtering strategies to ensure stability and efficiency. The first, high-latitude filtering, is done to control linear instability due to the converging meridions near the pole. This filter selectively damps the tendencies of fastest modes. Thus, on a uniform grid, the filter acts near the poles on the smallest scales. The second technique is the application of the Shapiro (1970) filter. This filter is applied globally to damp small-scale dispersive waves and to prevent computational nonlinear instability (Phillips, 1959) to occur. This report will examine the properties of these two filtering techniques on the stretched grid, and develop a stretched grid convolution filter applicable to controlling linear instability in high latitudes.

2 Stretched Grid GEOS GCM

Following the work of Fox-Rabinovitz et al. (1997), the stretched grid dynamical core was interfaced with the uniform grid physics package of the GEOS General Circulation Model (GCM). While the ultimate goal will be to perform the physics on the stretched grid itself, this more conservative approach was used to avoid unforseen problems within the parameterizations in regions of high resolution. In practice, a copy of the dynamic state variables (u, v, θ, q, p_s) are transformed (via cubic interpolation) to the uniform grid to force the physics packages. The *tendencies* of the dynamic state variables due to the physics are then transformed to the dynamics stretched grid to act as external diabatic forcing in the time integration scheme. As a result, the dynamics state is always updated and preserved on the stretched grid.

The generation of the stretched grid used for this study employs a cosine mapping function to smoothly create grid increments which vary with wavenumber 1 in the longitudinal direction, and increase to a maximum at the farthest pole in the latitudinal direction. These longitude and latitude grid increments are shown in Fig. 1. For this study, the uniform grid resolution is defined by a 2.5°x2.0° *lon-lat* grid (144x91 points). These points are re-distributed in longitude and latitude so as to produce uniform 1.0°x1.0° resolution over the eastern United States ($\sim$ 28N-48N, 100W-70W). Figure 2 shows the resulting 2-dimensional grid structure over the globe. Note that in the coarsest region (the South-East quadrant) an effective resolution of $\sim$ 5°x4° is used.

Starting from an arbitrary, uniform grid January simulation, initial conditions were transformed and balanced on the stretched grid to begin stretched grid forecasts. The top panel of Fig. 3 shows the initial zonal mean temperature distribution and the day 5 temperature change from the intitial condition. During this 5-day forecast, a stratospheric warming event has taken place (between day 4 and 5) which is associated with strong cross-polar flow. The bottom panel shows the temperature change and day 5 zonal wind at 0.2 mb from latitudes 50N to 90N (longitude 0 at bottom). We see that near the poles in the region of highest longitudinal resolution, computational small scale features have developed. This occurs even though the timestep chosen for the integration was adequately reduced to reflect the increased resolution in the area of interest. It was noted in Fox-Rabinovitz et al. (1997) that, even for the simple-physics Held-Suarez test, excessive polar noise developed when total stretching factors ($\frac{\Delta\lambda_{max}}{\Delta\lambda_{min}}$) became large ($\geq 16$). In those cases, *ad hoc* strengthening of the polar filters was required. It is clear from these results that, while the standard polar filtering technique is effective in preventing linear instability in many cases, it is not robust enough for use on the stretched grid for general applications.

3 Uniform Grid High-Latitude Filter

To understand why the standard high-latitude filtering technique is not adequate when using the stretched grid, we must first review the technique employed on the uniform grid. As pointed out in Suarez and Takacs (1995), polar Fourier filters in the Aries/GEOS dynamical core are applied to the *tendencies* of all prognostic variables. This is done to avoid linear computational instability due to the convergence of the meridians near the poles. The filter acts poleward of a critical latitude ϕ_c (nominally 45°), and its strength is gradually increased toward the pole by increasing the number of affected zonal wavenumbers and the amount by which they are damped.

Consider the linearized, one-dimensional shallow water equations with no mean flow given by:

$$\frac{\partial u}{\partial t} = -\frac{g}{a\cos\phi}\frac{\partial h}{\partial\lambda}\,, \tag{1}$$

$$\frac{\partial h}{\partial t} = -\frac{H}{a\cos\phi}\frac{\partial u}{\partial\lambda}\,. \tag{2}$$

Discretizing in space on a staggered C-grid, we may write

$$\frac{\partial u_{i+\frac{1}{2}}}{\partial t} = -\frac{g}{a\cos\phi}\left(\frac{h_{i+1}-h_i}{\Delta\lambda}\right) , \tag{3}$$

$$\frac{\partial h_i}{\partial t} = -\frac{H}{a\cos\phi}\left(\frac{u_{i+\frac{1}{2}}-u_{i-\frac{1}{2}}}{\Delta\lambda}\right) . \tag{4}$$

Here, $\Delta\lambda = \frac{2\pi}{\mathrm{IM}}$ and IM is the zonal dimension. Assuming wave solutions of the form:

$$u_{i+\frac{1}{2}}(t) = \hat{u}e^{\iota(k(i+\frac{1}{2})\Delta\lambda-\nu t)} , \tag{5}$$

$$h_i(t) = \hat{h}e^{\iota(ki\Delta\lambda-\nu t)} , \tag{6}$$

where i denotes the grid-space location in longitude and $\iota = \sqrt{-1}$, it can be shown that the frequency associated with each harmonic component k is given by

$$\nu = \pm\,\frac{2\sqrt{gH}}{a\cos\phi\Delta\lambda}\quad\sin(k\frac{\Delta\lambda}{2}) . \tag{7}$$

We see that the frequency increases as a function of wavenumber and as we approach the pole.

Using the leapfrog time scheme, linear stability requires that

$$\nu\Delta t \leq 1. \tag{8}$$

This forces restrictions on the timestep governed by

$$\Delta t \leq \frac{1}{2}\,\frac{a\cos\phi\Delta\lambda}{\sqrt{gH}}\quad\frac{1}{\sin(k\frac{\Delta\lambda}{2})} . \tag{9}$$

To eliminate the requirement that the timestep goes to zero as we approach the pole, a wavenumber-dependent filter, F_k, is applied to the time tendencies of the prognostic fields resulting in a modified frequency function given by

$$\nu = \pm\,F_k\,\frac{2\sqrt{gH}}{a\cos\phi\Delta\lambda}\quad\sin(k\frac{\Delta\lambda}{2}) . \tag{10}$$

By requiring that the frequency be no larger than ν_{MAX} (e.g., the unfiltered value associated with the shortest wavelength at the critical latitude ϕ_c), the functional form of F_k may be obtained:

$$F_k = \min\left[1, \left(\frac{\cos\phi}{\cos\phi_c}\,\frac{1}{\sin(k\frac{\Delta\lambda}{2})}\right)^n\right] . \tag{11}$$

Here, n is an arbitrary factor used by Suarez and Takacs (1995) to increase the strength of the filter. While not needed for these linear studies, it has proven beneficial to use $n = 2$ for the non-linear uniform grid GCM. Unless otherwise stated, results shown here were made using $n = 1$. It is important to remember that applying the filter in this manner simply *slows down* each harmonic component by an amount which produces linear stability. More precisely, the computational propogation speed of each zonal harmonic is adjusted to keep its transport to no more than 1 $\Delta\lambda$ per timestep. The filter has no impact on the magnitude nor energy of the harmonic.

Figures 4 and 5 show the filter function at latitudes 85N and 60N, respectively. For these results, the zonal dimension was set to IM=144 (corresponding to a 2.5° resolution). Near the pole (85N) the filter strength is quite strong with only wavenumbers 0-5 remaining untouched. However, away from the pole (60N) the filter is much weaker with only moderate damping even at the smallest scales. Also shown in Figs. 4 and 5 are the equivalent grid-space weighting coefficients at various longitudes obtained through convolution of the spectral filter functions. Since the grid is uniform, the weighting stencil is identical for each longitude location. For the strong spectral filter function near the pole, the convolution weights are quite broad in longitude and have a peak amplitude which is relatively small (0.3). Away from the pole where the filter strength is weak, the convolution weights resemble that of a Delta function whose amplitude is near 1.0 at the grid-point location and almost 0.0 elsewhere. The breadth of the convolution weights are thus intimately connected to the physical scale of the waves being filtered.

To illustrate the effect of filtering, a set of initial conditions consisting of the single harmonics 1, 3, 5, and 7 (see Fig. 6) is used. To benchmark this test, the integration is first run *without filters* by using a sufficiently small timestep which is linearly stable, Fig. 7. These single harmonics simply oscillate in time with no translational motion. The test is then repeated using a timestep comparable to that used for GCM simulations. Without filtering, instability occurs within a few iterations (not shown). Figure 8 shows the results from the uniform grid using the standard FFT polar filter described above. The filtering associated with latitude 85N was used for these runs. With tendency filtering, the solutions look quite similar to the non-filtered case with no discernable instabilities. Figure 9 compares the filtered and non-filtered solutions at longitude 0°, with additional wavenumbers 9 and 12 also shown. As the wavenumber increases, the frequency is increasingly slowed compared with the non-filtered run. Also, the frequencies for wavenumbers 7, 9, and 12 are identical for the filtered run since they are forced to be no greater than the maximum allowed value. However, the magnitude of the oscillation remains untouched, with no distortion of the waveform.

The experiment is then repeated using the stretched grid. The uniform 2.5° grid is stretched to 1° between longitudes 75E and 105E, Fig. 10, with initial conditions shown in Fig. 11. Figure 12 shows the results for the stretched grid using a sufficiently small timestep to ensure stability without filtering. The stretched grid solution is very similar to the uniform-grid solution, creating negligable distortion due to the stretching. The experiment is again repeated using a larger timestep comparable to that used for GCM simulations and thus requiring tendency filtering, Fig. 13. It is clear that the use of the standard FFT filter has created significant distortions of the pure waveforms and has affected the solution at all longitudes. In addition, significant small-scale features have been created even though linear stability has been achieved. Arbitrarily increasing the strength of the filter to $n = 2$ creates even further distortions, Fig. 14. A snapshot of the solution at 3 hours is shown in Fig. 15 clearly demonstrating the inability of the standard FFT filter to adequately control noise and prevent distortions on the stretched grid.

4 Stretched Grid High-Latitude Filter

Since the standard filtering technique is done in spectral space, it is clear that the functions upon which stability is based (the trigonometric zonal harmonics) must have the same relevance on the stretched grid for the filtering technique to be valid. Figure 16 depicts the single harmonic wavenumber 3 on the uniform grid (top panel) and on the stretched grid (center panel). Here, the term "wavenumber 3" is used to describe a field whose structure is repeated three times in the longitudinal direction. Using this definition we see that for each zonal harmonic k there is an associated geophysical scale whose wavelength L_k is given by:

$$L_k = \frac{2\pi a \cos\phi}{k} \; . \tag{12}$$

This physically-based wavelength is independent of any finite-resolution grid used to construct the field. Assuming this physically-based wave propogates uniformly in the zonal direction, the filter strength required to slow it down must clearly be a function of the local zonal grid increment just as it is a function of latitude (i.e., the required strength to restrict transport to no more than 1 $\Delta\lambda$ per timestep would need to be greater in an area of high resolution than in an area of coarse resolution). However, as shown above for the standard filtering technique, there is no longitudinal dependence on the filter strength F_k. Moreover, since the FFT implicitly assumes a uniform grid distribution, the FFT interprets this wavenumber 3 example as a field which is made up of both longer and shorter wave components (Fig. 16, bottom panel). The varying strengths of the filter as defined by (11) for these wavenumbers would be misapplied if the intent was to filter the *geophysical* scale associated with wavenumber 3.

The top panel of Figure 17 shows the FFT harmonic decomposition of the wavenumber 3 example for both the uniform grid and the stretched grid. Interestingly, the wavenumber 3 harmonic is almost completely missing from the stretched grid interpretation. Instead we see a spread of harmonics to either side of the actual input wavenumber. The bottom panel of Fig. 17 repeats this analysis for each wavenumber from 0 to IM/2. Each single harmonic wave component is projected onto the strethed grid, and then used as input to the FFT analysis. As before, each component is interpreted as having both longer waves and shorter waves, with little energy in the actual wavenumber used as input.

Figure 18 examines the convolution weights obtained from the standard FFT filter but applied on the stretched grid. The top panel, as before, shows the spectral filter function independent of longitude. The bottom panel of Fig. 18 shows the convolution weights plotted on the stretched grid. We see that the peak amplitude of the weights is constant in longitude. However, in the fine-resolution region the convolution weights have narrowed in longitude while in the coarse-resolution region they have broadened. This implies that the effect of the standard filtering technique on the stretched grid will be to filter less in the fine-resolution region and filter more in the coarse-resolution region, exactly *opposite* to that required from previous considerations.

It has become clear that to accurately filter on a stretched grid, we must first determine the stretched grid basis functions upon which the model solutions may be projected. We again start by writing the discretized linear shallow water equations for the stretched grid:

$$\frac{\partial u_{i+\frac{1}{2}}}{\partial t} = -\frac{g}{a\cos\phi}\left(\frac{h_{i+1}-h_i}{\Delta\lambda_{i+\frac{1}{2}}}\right) , \tag{13}$$

$$\frac{\partial h_i}{\partial t} = -\frac{H}{a\cos\phi}\left(\frac{u_{i+\frac{1}{2}}-u_{i-\frac{1}{2}}}{\Delta\lambda_i}\right) . \tag{14}$$

Here, $\Delta\lambda_{i+\frac{1}{2}}$ is the distance in longitude between mass points, and

$$\Delta\lambda_i = \frac{\Delta\lambda_{i+\frac{1}{2}}+\Delta\lambda_{i-\frac{1}{2}}}{2} . \tag{15}$$

Using (13) and (14), the wave equation is formed given by:

$$\frac{\partial^2 h_i}{\partial t^2} = \frac{gH}{(a\cos\phi)^2}\left[\frac{h_{i+1}-h_i}{\Delta\lambda_i\Delta\lambda_{i+\frac{1}{2}}} - \frac{h_i-h_{i-1}}{\Delta\lambda_i\Delta\lambda_{i-\frac{1}{2}}}\right] . \tag{16}$$

Assuming a solution of the form:

$$h_i(t) = \hat{h}_i e^{-\iota\nu t} , \tag{17}$$

we find

$$
\begin{aligned}
\frac{-\nu^2(a\cos\phi\Delta\lambda)^2}{gH}\,\hat{h}_i &= \left(\frac{\Delta\lambda^2}{\Delta\lambda_i\Delta\lambda_{i+\frac{1}{2}}}\right)\,\hat{h}_{i+1} \\
&- 2\left(\frac{\Delta\lambda^2}{\Delta\lambda_{i+\frac{1}{2}}\Delta\lambda_{i-\frac{1}{2}}}\right)\,\hat{h}_i \\
&+ \left(\frac{\Delta\lambda^2}{\Delta\lambda_i\Delta\lambda_{i-\frac{1}{2}}}\right)\,\hat{h}_{i-1}\ , \qquad (18)
\end{aligned}
$$

where $\Delta\lambda = \frac{2\pi}{\mathrm{IM}}$. Note that for the uniform grid ($\Delta\lambda_i = \Delta\lambda$) the weights used in (18) simply become 1, -2, 1. Defining:

$$
r_i = \frac{\Delta\lambda^2}{\Delta\lambda_{i+\frac{1}{2}}\Delta\lambda_{i-\frac{1}{2}}}\ , \qquad (19)
$$

$$
r_i^+ = \frac{\Delta\lambda^2}{\Delta\lambda_i\Delta\lambda_{i+\frac{1}{2}}}\ , \qquad (20)
$$

$$
r_i^- = \frac{\Delta\lambda^2}{\Delta\lambda_i\Delta\lambda_{i-\frac{1}{2}}}\ , \qquad (21)
$$

we may write (18) in matrix form as:

$$
\begin{pmatrix}
-2r_1 & r_1^+ & & & r_1^- \\
r_2^- & -2r_2 & r_2^+ & & \\
 & r_3^- & \ddots & \ddots & \\
 & & \ddots & -2r_{\mathrm{IM\text{-}1}} & r_{\mathrm{IM\text{-}1}}^+ \\
r_{\mathrm{IM}}^+ & & & r_{\mathrm{IM}}^- & -2r_{\mathrm{IM}}
\end{pmatrix}
\hat{\mathbf{h}} = \lambda\,\hat{\mathbf{h}}\ , \qquad (22)
$$

where λ is the eigenvalue associated with the eigenfrequency ν:

$$
\lambda = -\frac{\nu^2(a\cos\phi\Delta\lambda)^2}{gH}\ . \qquad (23)
$$

From (22) and (23), we may compute the eigenvalues (or eigenfrequencies) and corresponding eigenvectors associated with the stretched grid (see Appendix for detail). Figure 19 shows the eigenvalues computed by solving (22) for both the uniform grid and the stretched grid, in addition to the analytic uniform grid solution associated with (7). Here we have ordered the eigenvalues by magnitude. For the uniform grid, the analytic and numerical solutions are indistinguishable. For the stretched grid, we see a significant increase in the magnitude of the eigenvalues associated with the highest mode index (smallest scales).

The eigenvectors associated with a sampling of modes are shown in Fig. 20 for the uniform grid and Fig. 21 for the stretched grid. The uniform grid solutions are simply discretized sines and cosines, analogous to the analytic solution. The eigenvectors for the stretched grid are similar for the low-index (slow) modes. However, as the mode index (or eigenfrequency) increases the structure of the eigenvector is confined to smaller and smaller regions. For the highest eigenfrequency, the eigenvector is totally concentrated in the finest resolution area.

By ordering the eigenvalues and associated eigenvectors in this manner, a filter may be constructed to selectively damp those modes whose associated eigenfrequencies are faster than some critical value. Using (23) we see that

$$\nu = \pm \frac{|\lambda|^{\frac{1}{2}} \sqrt{gH}}{a \cos \phi \Delta\lambda} \ . \tag{24}$$

As in the uniform grid case, the maximum frequency allowed will be defined as the unfiltered frequency associated with the shortest wave at the critical latitude ϕ_c:

$$\nu_{\mathrm{MAX}} = \frac{2\sqrt{gH}}{a \cos \phi_c \Delta\lambda_{\mathrm{min}}} \ . \tag{25}$$

Requiring that the filtered frequency be no faster than the maximum frequency allowed,

$$F\ \nu \leq \nu_{\mathrm{MAX}} \ , \tag{26}$$

the filter function for the stretched grid becomes:

$$F = \min \left[1, \frac{2\Delta\lambda}{|\lambda|^{\frac{1}{2}} \Delta\lambda_{\mathrm{min}}} \frac{\cos\phi}{\cos\phi_c} \right] \ . \tag{27}$$

4.1 Convolution Filter

To construct the stretched grid convolution filter, consider for example the height field defined by a vector array $\mathbf{h}$ constructed from the set of modes found in Section 4:

$$\mathbf{h} = \mathbf{M}\mathcal{A} \ , \tag{28}$$

where $\mathbf{M}$ are the stretched grid modes or eigenvectors and $\mathcal{A}$ are the mode projection amplitudes. The amplitudes may be explicitly obtained by

$$\mathcal{A} = \mathbf{M}^{-1}\ \mathbf{h} \ . \tag{29}$$

A new set of amplitudes are now created by multiplying (29) by a diagonal matrix $\mathbf{F}$ defined by the convolution filter function (27):

$$\mathcal{A}^F \equiv \mathbf{F}\ \mathcal{A} = \mathbf{F}\ \mathbf{M}^{-1}\ \mathbf{h} \ . \tag{30}$$

The reconstructed filtered field, $\mathbf{h}^F$, is therefore given by:

$$\mathbf{h}^F \equiv \mathbf{M}\ \mathcal{A}^F = \underbrace{\mathbf{M}\ \mathbf{F}\ \mathbf{M}^{-1}}_{\text{Weights in Grid Space}}\ \mathbf{h}\ . \tag{31}$$

The weights obtained in grid space are analogous to the weights obtained through convolution of the standard FFT for the uniform grid. Through convolution we may now examine in spectral space the response of these weights as a function of longitude. The top panel of Fig. 22 shows the spectral response of the stretched grid convolution filter for various longitude locations, while the bottom panel shows the grid space weighting coefficients. We see that the amplitude of the coefficients is now a function of longitude while the breadth of the stencil is constant. This is exactly opposite to that obtained by the use of the standard FFT filter applied to the stretched grid, with the impact being that the strongest filtering now takes place in the region of highest resolution. The results from using the stretched grid convolution filter are shown in Fig. 23. The stretched grid convolution filter successfully prevents linear instability with no distortion of the waveforms nor generation of additional small scale features.

4.2 GEOS GCM Results

Having seen the effectiveness of using the stretched grid convolution filter in simple off-line, gravity wave test cases, we now proceed to analyze its performance within the GEOS GCM. For this test, the forecast experiment described in Section 2 is repeated by replacing the standard FFT polar filtering technique with that of the stretched grid convolution filter. Figure 24 once again shows the initial zonal mean temperature distribution and the day 5 temperature change, as well as the 0.2 mb day 5 temperature change and zonal wind fields. Compared with Fig. 3, the stratospheric warming event is again simulated but with no evidence of small-scale noise near the polar, high-resolution region. It should be noted that the noise generated with the standard filtering technique was primarily evident at high stratospheric altitudes where the wind field is particularly strong. At lower levels the standard filter and the stretched grid convolution filter produce very similar results. Figure 25 shows the sea-level pressure and 300-mb height fields at day 5 for the two simulations. The two solutions are virtually identical with no evidence of noise in either case.

4.3 Uniform Grid Interpretation

While the preceeding sections derived exactly the proper filter function for the linearized shallow water equations on a stretched grid, it is possible to approximate this solution through a uniform grid interpretation. Recall from Section 3 that the filter function derived for the uniform grid for $n = 1$ was given by

$$F_k = \min\left[1, \left(\frac{\cos\phi}{\cos\phi_c}\ \frac{1}{\sin(k\frac{\Delta\lambda}{2})}\right)\right] \ , \tag{32}$$

for $k = 0, \frac{\mathrm{IM}}{2}$. This may be rewritten as:

$$F_{i,k'} = \min\left[1, \left(\frac{a\cos\phi\Delta\lambda_i}{a\cos\phi_c\Delta\lambda_{\min}}\ \frac{1}{\sin(k'\frac{\Delta\lambda_i}{2})}\right)\right] \ , \tag{33}$$

for

$$k' = 0, \frac{\mathrm{N}_i}{2} \ , \tag{34}$$

$$\mathrm{N}_i = \frac{2\pi}{\Delta\lambda_i} \ . \tag{35}$$

We see that for the uniform grid, $\Delta\lambda_i = \frac{2\pi}{\mathrm{IM}}$, (32) and (33) are identical. However, for the stretched grid we define N_i at each longitude location as the number of points a uniform grid would have assuming a uniform resolution of $\Delta\lambda_i$. This will produce a uniform grid filter function which, through convolution, may be represented by the grid-space weighting coefficients. The stretched grid weighting stencil may then be constructed by simply interpolating the uniform grid stencil to the stretched grid locations.

The top panel of Fig. 26 shows the grid-space weighting coefficients obtained using this empirical method, while the bottom panel shows the differences compared with the eigenvalue method. The empirical method produces coefficients very similar to the eigenvalue method, with the resulting simulation shown in Fig. 27. This implies that the stretched grid convolution filter developed in Section 4.1 acts to treat each *local* $\Delta\lambda_i$ as if it were *global*, and constructs a filter function based on a uniform grid of that resolution. Interestingly the minor differences which are obtained using this empirical method are ultimately pathological giving rise to instabilities as shown in Fig. 28 after 30 hours of simulation. However, as will be seen in the next section, this technique can be useful to analyze the impact of arbitrary uniform grid filter response functions applied to a stretched grid.

5 Global Shapiro Filter

As previously noted, the uniform grid GEOS GCM also employs the Shapiro (1970) filter to globally damp small-scale dispersive waves. This filter also prevents computational nonlinear instability (Phillips, 1959) to occur. The Shapiro filter is applied as a *tendency* to the winds, potential temperature, and tracers (including specific humidity). Thus, only a fraction of the full Shapiro filter is incorporated at each time step. This is done to reduce dynamical imbalances and diabatic responses caused by the filter.

The Shapiro filter tendency for a quantity q is defined by

$$\left(\frac{\partial q}{\partial t}\right)_{\mathrm{SF}} = \frac{q^F - q}{\tau} \;, \tag{36}$$

Here q and q^F are the unfiltered and filtered quantities, and τ is an adjustable timescale. For the uniform grid GEOS GCM, τ is set to 1.5 hours which effectively removes the smallest two-grid interval wave in approximately 6 hours. The filter is applied separately in the longitudinal and latitudinal direction using

$$q^F_{i,j} = [1 - (F^2_\phi)^n]\,[1 - (F^2_\lambda)^n]\; q_{i,j} \;, \tag{37}$$

where

$$\begin{aligned} F^2_\lambda(q_{i,j}) &= -\frac{1}{4}(q_{i+1,j} - 2q_{i,j} + q_{i-1,j}) \;, \\ F^2_\phi(q_{i,j}) &= -\frac{1}{4}(q_{i,j+1} - 2q_{i,j} + q_{i,j-1}) \;, \end{aligned} \tag{38}$$

and n is the Shapiro filter order/2. At 2.5°x2° resolution the GEOS GCM uses an 8th-order (n=4) filter. Lower-order filtering corresponds to stronger damping.

We may examine the Shapiro filter response function in one dimension by assuming a wave solution defined by

$$q_i = \hat{q}_k \; e^{\imath k i \Delta\lambda} \;. \tag{39}$$

Doing so we find

$$\hat{q}^F_k = 1 - \sin^{2n}(k\frac{\Delta\lambda}{2}) \;. \tag{40}$$

The left-hand column of Fig. 29 shows the frequency response for the 8th-order filter on a 2.5° uniform resolution grid as well as the grid space weights at selected longitudes obtained through convolution. We see that the grid space averaging is very local (only 9 grid points) and produces a sharp delineation between the small scales which are heavily filtered and the longest scales which are virtually untouched. The center column of Fig. 29 shows the response of the standard technique described above but applied to the stretched grid. In this case the basic local stencil is simply used without concern for the non-uniform mesh.

Due to the success of the uniform grid interpretation in approximating the convolution weights obtained by the eigenvalue method for the stretched grid high-latitude filter, it is useful to employ this technique to estimate the proper stretched grid convolution weights derived from the uniform grid Shapiro filter frequency response. The right-hand panel of Fig. 29 shows the results from assuming that each *local* $\Delta\lambda_i$ was *globally* uniform. The convolution weights associated with the Shapiro filter response for each implied uniform resolution were then interpolated to the actual stretched grid locations. The frequency response associated with these empirically derived coefficients was then plotted for selected longitude locations. Due to the very local nature of the Shapiro filter and the filter response's non-dependency on critical wavelengths, very little impact is seen as a result of the non-uniform grid. This is significantly different than the impact seen for the high-latitude filter case, Fig. 22, where longitudinal locality greatly influenced filter strength. As a result of this analysis in addition to empirical evidence from numerous stretched grid GCM simulations and the greater efficiency of the standard algorithm, no obvious advantage is realized by using the (empirical) eigenvalue method for the global Shapiro filter.

6 Conclusion

In this report the filtering characteristics of a stretched grid GCM have been reviewed. It was shown that using the standard FFT polar filtering technique, as performed by Fox-Rabinovitz et al. (1997) for the stretched grid Held-Suarez dynamics benchmark, computational small-scale noise is generated near the poles in the region of high longitudinal resolution. While this noise is associated with high wind speeds in the stratospheric domain, Fox-Rabinovitz et al. found similar problems when total stretching factors were large (≥ 16). For those cases, *ad hoc* strengthening of the filter coefficients were used to control stability.

A review of the standard high-latitude filtering procedure was made and an examination of the physical scales associated with the filter were analyzed on both the uniform grid and the stretched grid. It was shown that the implicit assumption of a uniform grid within the FFT algorithm results in a misrepresentation of the zonal harmonic composition of the input field. Standard filter strengths which are derived from uniform grid considerations and stability analyses are thus misapplied to the stretched grid harmonic decomposition, resulting in weaker filtering within the high resolution region and stronger filtering in the coarse resolution region. This is opposite to the requirement of stronger filtering in areas of high resolution.

A new filtering technique has been developed which accurately accounts for the non-uniform grid by computing the eigenvectors and eigenfrequencies associated with the stretching. It is shown that the convolution of the required damping function within mode space yields grid-spaced weights which can be efficiently used to perform the filtering without distortion. Offline tests showed that the stretched grid convolution filter correctly filtered more in the high resolution region and less in the coarse resolution region. Online GCM experiments further showed that computational small-scale noise was no longer generated in the region of highest longitudinal resolution near the poles. Away from high latitudes, no adverse effects from using the stretched grid convolution filter were seen. In the limit that the stretched grid becomes uniform, this technique reduces to the standard uniform grid filter.

In addition to the complete eigenvalue/eigenvector solution, an empirical method was developed which treats each *local* $\Delta\lambda_i$ as if it were *global*. The convolution weights associated with the filter frequency response for the implied uniform resolution are then interpolated to the actual stretched grid locations. This empirical estimation of the convolution weights for a stretched grid was used to analyze the impact of applying the Shapiro filter on the stretched grid. It was shown that due to the Shapiro filter's very local grid stencil (9 points for the 8th-order filter), the standard application of the Shaprio filter produced very small differences compared with the (empirical) eigenvector method. Due to the greater efficiency of the standard algorithm, no obvious advantage is realized by using the (empirical) eigenvector method for global filtering.

Acknowledgements
This work was supported by the Global Atmospheric Modeling and Analysis Program, NASA/Office of Earth Science.

Appendix

Linear Algebra Aspects of the Stretched Grid Convolution Filter

The stretched grid convolution filter requires the eigenvalues and eigenvectors of a non-symmetric matrix (which we define here as $\mathbf{R}$) from (22). The matrix $\mathbf{R}$ is a tridiagonal matrix with the addition of the two corner elements r^+_{IM} and r^-_1. It has several interesting properties. From (19), (20), and (21) it is clear that all row sums are zero. That is, $\forall i : -2r_i + r_i^+ + r_i^- = 0$, or in matrix form,

$$\mathbf{Rc} = \mathbf{0} \tag{41}$$

where $\mathbf{c}$ is a vector of constant elements $\mathbf{c} = (c, c, \ldots, c)^T$. In other words $\mathbf{R}$ is singular. From the same definitions (19), (20), and (21) it is easily shown the product of the ratios $\frac{r_i^+}{r_i^-}$ is unity:

$$\prod_{i=1}^{n} \frac{r_i^+}{r_i^-} = 1 \tag{42}$$

since every $\Delta\lambda_i$, $\Delta\lambda_{i+\frac{1}{2}}$ and $\Delta\lambda_{i-\frac{1}{2}}$ appears in both the numerator and the denominator.

If (19), (20), and (21) are all multiplied through by $\Delta\lambda_i$, or equivalently, (22) is multiplied on the left by

$$\mathbf{\Lambda} = \begin{bmatrix} \Delta\lambda_1 & & & \\ & \Delta\lambda_2 & & \\ & & \ddots & \\ & & & \Delta\lambda_{\mathrm{IM}} \end{bmatrix} \tag{43}$$

a generalized eigenvalue problem containing a symmetric left-hand side $\hat{\mathbf{R}} = \mathbf{\Lambda R}$ side can be obtained:

$$\hat{\mathbf{R}}\,\hat{\mathbf{h}} \;=\; \lambda\,\mathbf{\Lambda}\,\hat{\mathbf{h}}\ . \tag{44}$$

It would therefore be straightforward to use a generalized eigen-solver for symmetric matrices to solve the eigenvalue problem. But the problem can be further simplified. Since both $\hat{\mathbf{R}}$ and $\mathbf{\Lambda}$ are real and symmetric, it is clear that all λ are real. This means that $\mathbf{R}$ is symmetrizable, that is, a similarity transform can be applied to $\mathbf{R}$ to create a symmetric matrix with the same eigenvalues:

$$\mathbf{Z}\ \mathbf{R}\ \mathbf{Z}^{-1} = \mathbf{S} = \mathbf{S}^T\ . \tag{45}$$

In order to find $\mathbf{Z}$ by construction, consider the diagonal matrix

$$\mathbf{Z} = \begin{bmatrix} \delta_1 & & & \\ & \delta_2 & & \\ & & \ddots & \\ & & & \delta_{\mathrm{IM}} \end{bmatrix}\ . \tag{46}$$

Clearly, $\mathbf{Z}^{-1}$ is also a diagonal matrix with $\frac{1}{\delta_i}$ on the diagonal.[1] If the similarity transform is applied using this $\mathbf{Z}$, the result is a matrix with the same structure as $\mathbf{R}$:

$$\mathbf{S} = \mathbf{Z}\ \mathbf{R}\ \mathbf{Z}^{-1} = \begin{bmatrix} -2r_1 & \frac{\delta_1}{\delta_2} r_1^+ & & & \frac{\delta_1}{\delta_{\mathrm{IM}}} r_1^- \\ \frac{\delta_2}{\delta_1} r_2^- & -2r_2 & \frac{\delta_2}{\delta_3} r_2^+ & & \\ & \frac{\delta_3}{\delta_2} r_3^- & \ddots & \ddots & \\ & & \ddots & -2r_{\mathrm{IM}-1} & \frac{\delta_{\mathrm{IM}-1}}{\delta_{\mathrm{IM}}} r_{\mathrm{IM}-1}^+ \\ \frac{\delta_{\mathrm{IM}}}{\delta_1} r_{\mathrm{IM}}^+ & & & \frac{\delta_{\mathrm{IM}}}{\delta_{\mathrm{IM}-1}} r_{\mathrm{IM}}^- & -2r_{\mathrm{IM}} \end{bmatrix}\ . \tag{47}$$

This matrix is symmetric if, and only if, the elements r_i^+ and r_i^- are non-zero, and the following conditions are satisfied:

$$\delta_{i+1}{}^2 = \frac{r_i^+}{r_{i+1}^-} \delta_i{}^2\ . \tag{48}$$

The conditions (48) wrap around (i.e., $\delta_1{}^2 = \frac{r_{\mathrm{IM}}^+}{r_1^-} \delta_{\mathrm{IM}}$) and can only be satisfied if

$$\frac{r_1^+ r_2^+ \cdots r_{\mathrm{IM}}^+}{r_1^- r_2^- \cdots r_{\mathrm{IM}}^-} = 1\ . \tag{49}$$

From (42) we already know this to be the case for the matrix $\mathbf{R}$. One degree of freedom is left to set, for example, $\delta_1 = 1$. Thus, with a simple similarity transform, a symmetric matrix

[1] It is assumed that the δ_i are non-zero.

can be obtained which is more efficient to factorize[2] than the original $\mathbf{R}$. It also improves the algorithm by indicating that the eigenvalues are necessarily real — a non-symmetric eigensolver might return very small imaginary components due to round-off errors. Finally, the eigen-decomposition of a symmetric matrix yields orthogonal eigenvectors $\mathbf{Q}$,

$$\mathbf{Q}^T\ \mathbf{S}\ \mathbf{Q} = \mathbf{diag}(\lambda_1, \lambda_2, \ldots, \lambda_{\mathrm{IM}}) \tag{50}$$

which can be a considerable advantage.

Equation (41) indicates that $\mathbf{R}$ has a zero eigenvalue, i.e., $\lambda_1 = 0$. Although most eigensolvers can handle such a case, it is conceivable that floating point errors can result. In order to further stabilize the algorithm, it may be worthwhile to remove the zero eigenvalue by the following technique. The eigenvector to the zero eigenvalue of $\mathbf{R}$ is clearly $\mathbf{c}$, a vector of constants, as shown in (41). The equation

$$\mathbf{R}\ \mathbf{c} = \mathbf{Z}^{-1}\ \mathbf{S}\ \mathbf{Z}\mathbf{c} = \mathbf{0} \tag{51}$$

indicates that $\mathbf{y} = \mathbf{Z}\mathbf{c}$ is the eigenvector of $\mathbf{S}$ corresponding to its zero eigenvalue. Assuming a normalized $\mathbf{y}$ it is possible to create an orthonormal basis,

$$\mathbf{Y} = \left[\mathbf{y}\ \tilde{\mathbf{Y}}\right] \tag{52}$$

where $\tilde{\mathbf{Y}}$ can be constructed iteratively from Gram-Schmidt orthogonalization. Thus a second similarity transformation can be applied on $\mathbf{S}$ using $\tilde{\mathbf{Y}}$:

$$\begin{aligned}
\mathbf{Y}^T\ \mathbf{S}\ \mathbf{Y} &= \begin{bmatrix} \mathbf{y}^T \\ \tilde{\mathbf{Y}} \end{bmatrix} [\mathbf{S}] \left[\mathbf{y}\ \tilde{\mathbf{Y}}\right] && (53) \\
&= \begin{bmatrix} \mathbf{y}^T\mathbf{S}\mathbf{y} & \mathbf{y}^T\mathbf{S}\tilde{\mathbf{Y}} \\ \tilde{\mathbf{Y}}^T\mathbf{S}\mathbf{y} & \tilde{\mathbf{Y}}^T\mathbf{S}\tilde{\mathbf{Y}} \end{bmatrix} && (54) \\
&= \begin{bmatrix} 0 & \mathbf{0}^T \\ \mathbf{0} & \tilde{\mathbf{S}} \end{bmatrix}. && (55)
\end{aligned}$$

Note, for example, that $\mathbf{y}^T\mathbf{S}\tilde{\mathbf{Y}} = \mathbf{y}^T\mathbf{S}^T\tilde{\mathbf{Y}} = (\mathbf{S}\mathbf{y})^T\tilde{\mathbf{Y}} = \mathbf{0}^T$. This similarity transform ensures that $\tilde{\mathbf{S}}$ is also symmetric and contains all the eigenvalues of $\mathbf{S}$ except the zero eigenvalue corresponding to eigenvector $\mathbf{y}$. The symmetric matrix $\tilde{\mathbf{S}}$ has the eigen-decomposition,

[2] For example, with the LAPACK routine `dsyev`.

$$\tilde{\mathbf{Q}}^T \ \tilde{\mathrm{S}} \ \tilde{\mathbf{Q}} = \mathbf{diag}(\lambda_2, \ldots \lambda_{\mathrm{IM}}) \ . \tag{56}$$

From (53) and (56) it is straightforward to show that the eigenvectors of the non-zero[3] eigenvalues are $\tilde{\mathbf{Y}}\tilde{\mathbf{Q}}$. Thus the full set of eigenvectors of $\mathbf{S}$ is:

$$\mathbf{Q} = \left[\begin{array}{cc} \mathbf{y} & \tilde{\mathbf{Y}}\tilde{\mathbf{Q}} \end{array} \right] . \tag{57}$$

It is now possible to specify the eigen-decomposition of $\mathbf{R}$ in terms of all the components of the fully stabilized eigen-solver:

$$\begin{aligned} \mathbf{M}^{-1}\mathbf{R}\mathbf{M} &= \mathbf{diag}(0, \lambda_2, \ldots \lambda_{\mathrm{IM}}) & (58) \\ &= \mathbf{Q}^T\mathbf{S}\mathbf{Q} & (59) \\ &= \left[\begin{array}{c} \mathbf{y}^T \\ \tilde{\mathbf{Q}}^T\tilde{\mathbf{Y}}^T \end{array} \right] \mathbf{Z}^{-1}\mathbf{R}\mathbf{Z} \left[\begin{array}{cc} \mathbf{y} & \tilde{\mathbf{Y}}\tilde{\mathbf{Q}} \end{array} \right] . & (60) \end{aligned}$$

Thus, with the eigenvectors $\tilde{\mathbf{Q}}$ of $\tilde{\mathbf{S}}$, the normalized eigenvector $\mathbf{y}$, the set of constructed orthonormal vectors $\tilde{\mathbf{Y}}$, and the diagonal matrix $\mathbf{Z}$, it is possible to recreate the eigenvectors $\mathbf{M}$ of $\mathbf{R}$:

$$\mathbf{M} = \mathbf{Z} \left[\begin{array}{cc} \mathbf{y} & \tilde{\mathbf{Y}}\tilde{\mathbf{Q}} \end{array} \right] \tag{61}$$

which are required in the stretched grid convolution filter.

[3]The proof is omitted here that all other eigenvalues of $\mathbf{S}$ are non-zero.

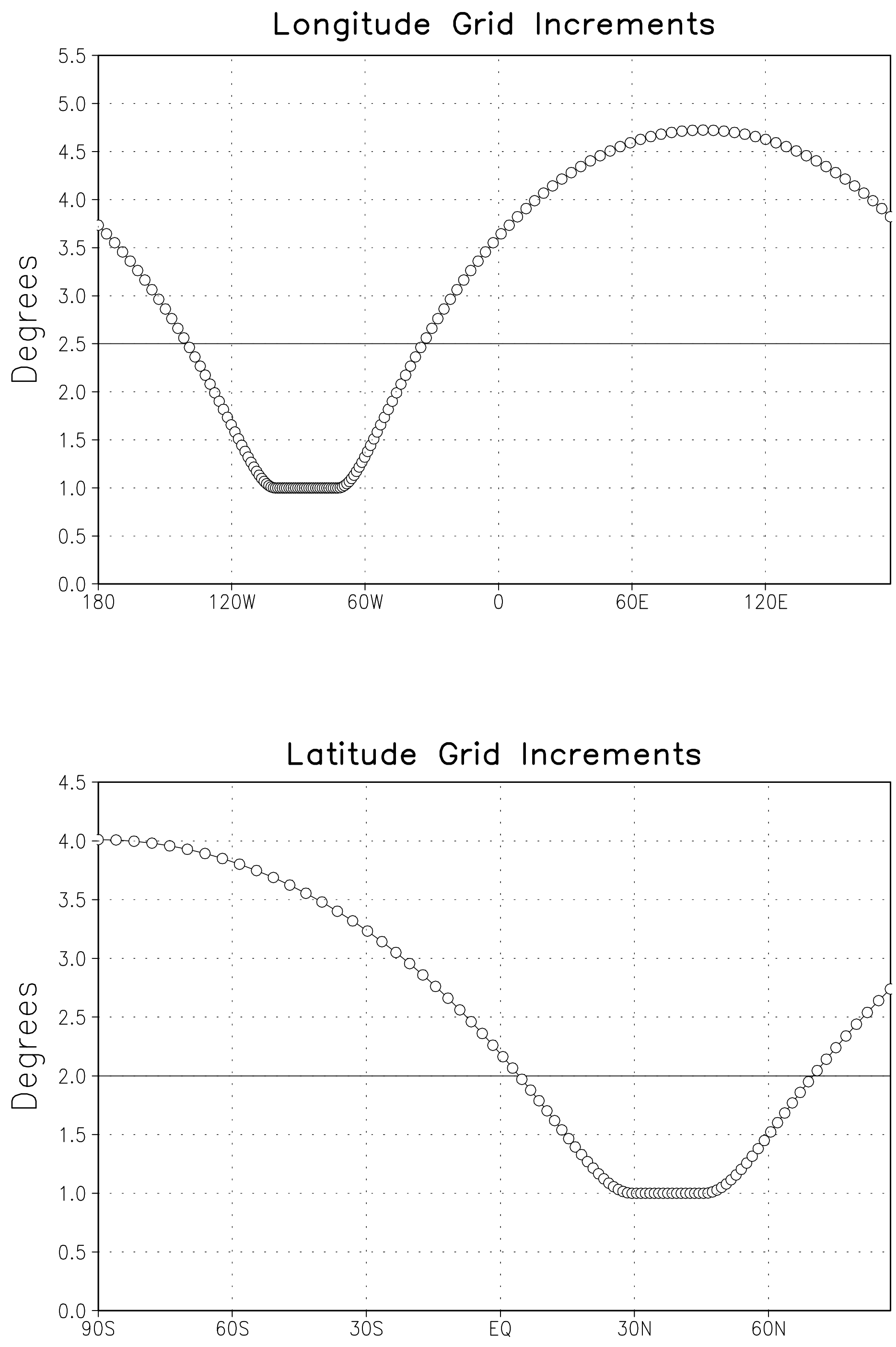

Figure 1: Longitude and Latitude Grid Increments using stretched grid.

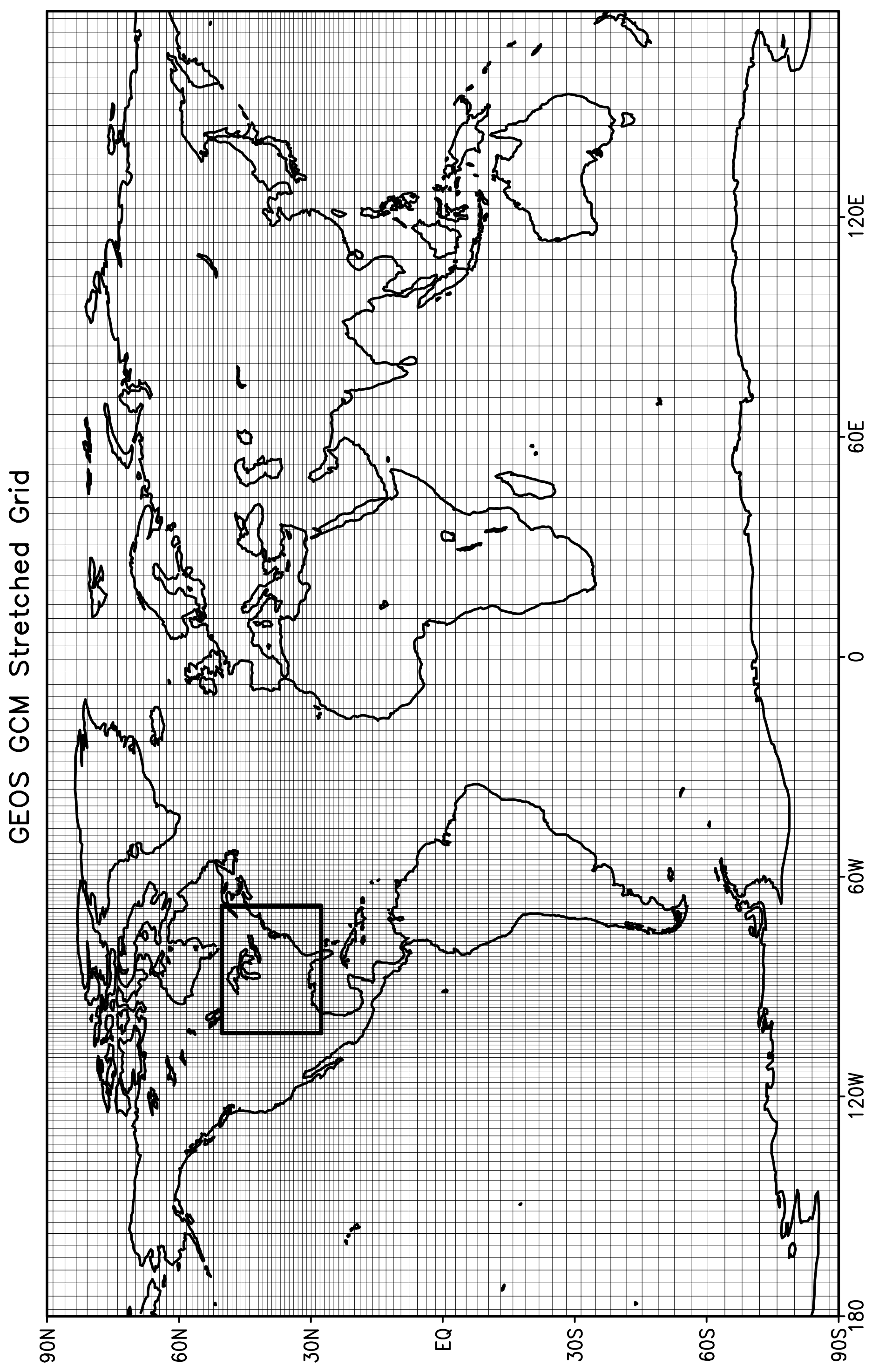

Figure 2: Stretched grid structure used for GCM experiments.

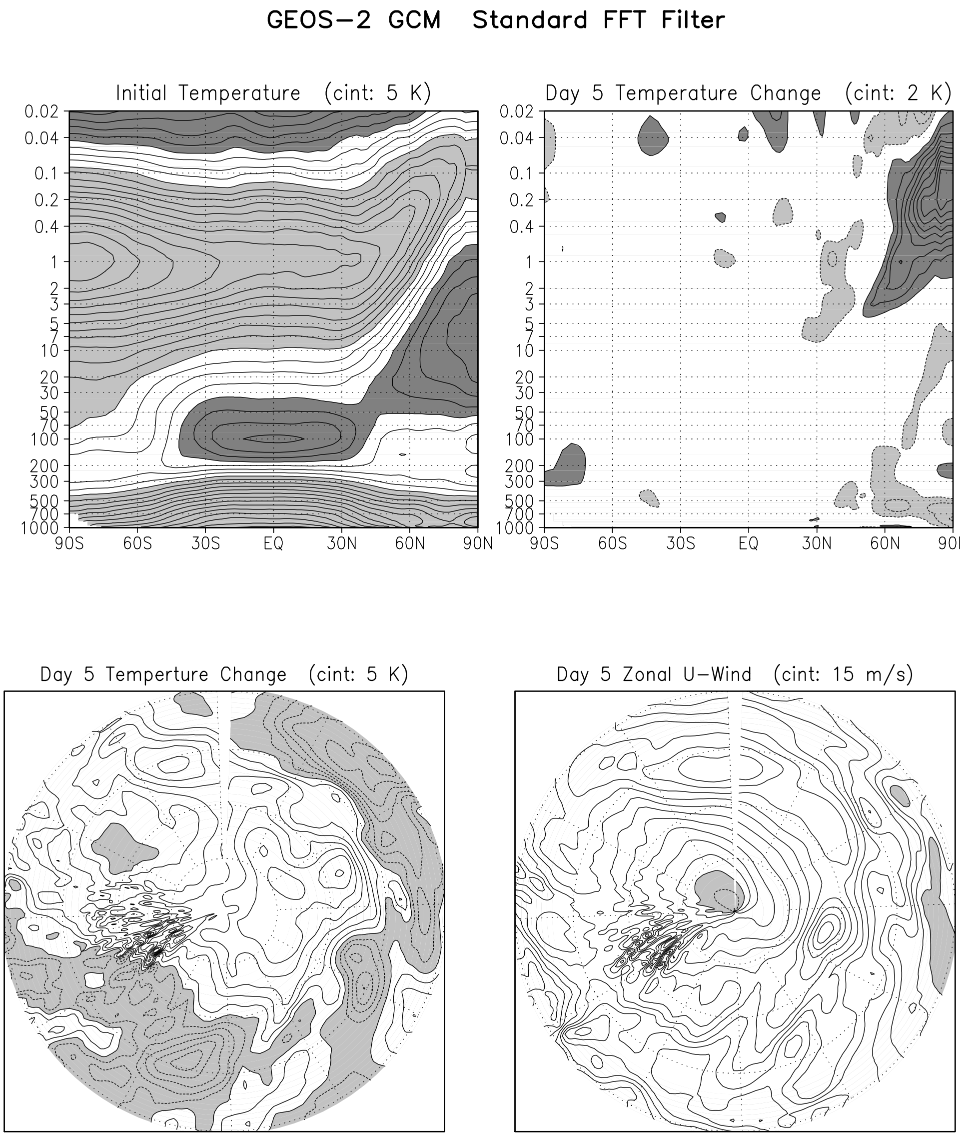

Figure 3: Initial temperature and Day 5 temperature change (top panel), and 0.2 mb temperature change and zonal wind field (bottom panel) using the standard FFT filter on the stretched grid.

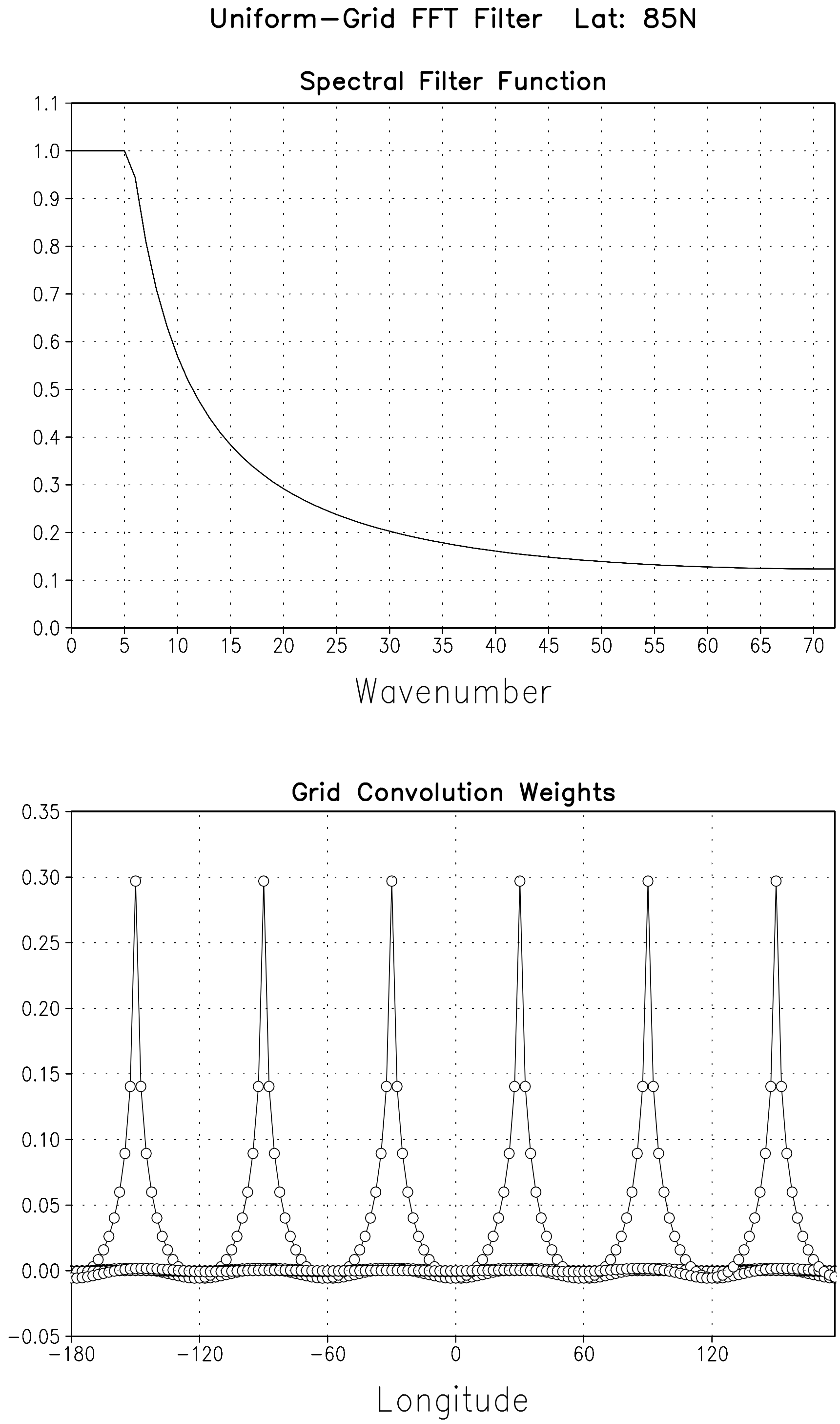

Figure 4: Filter function and grid-space weighting coefficients at 85N for uniform grid.

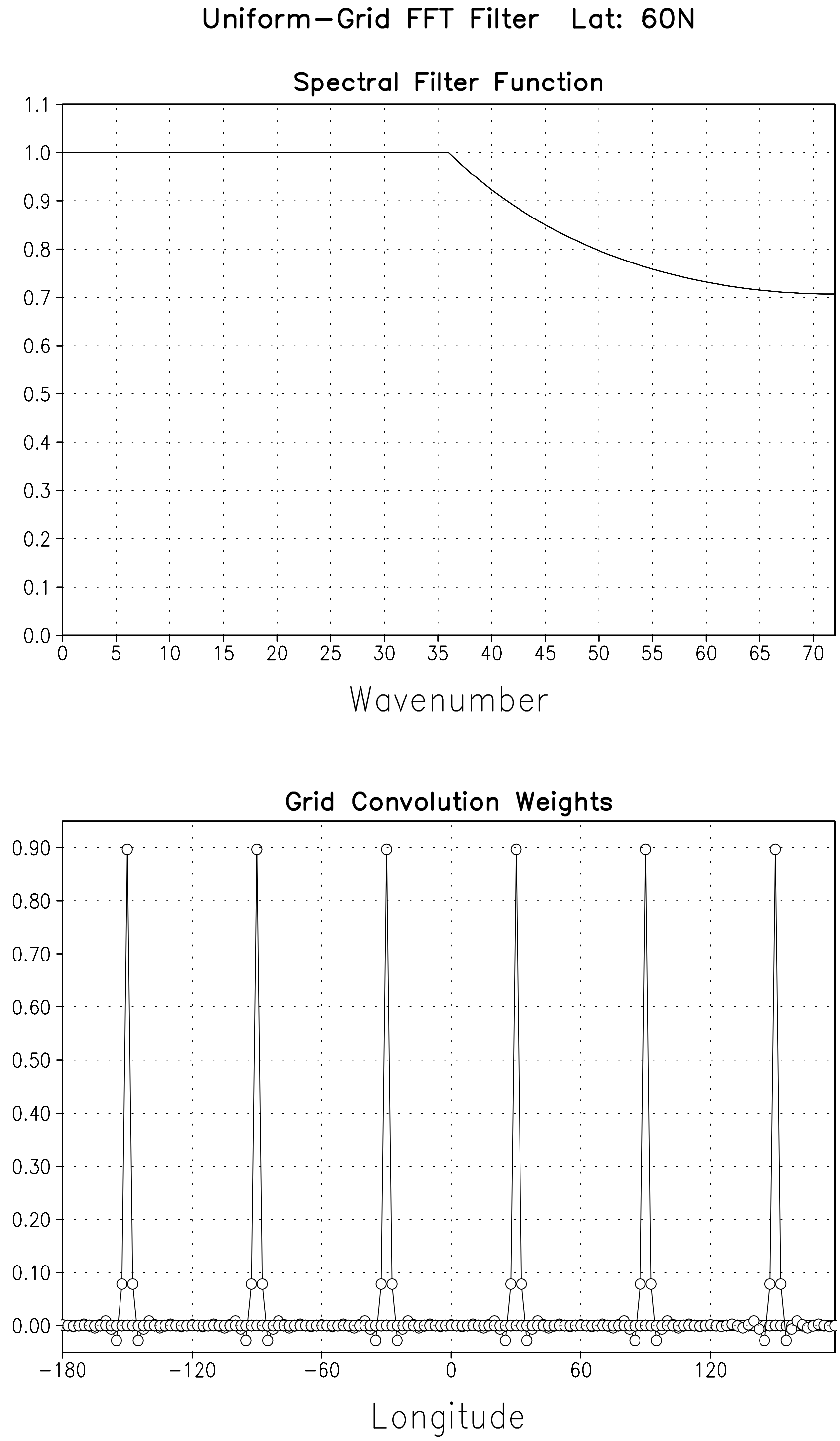

Figure 5: Filter function and grid-space weighting coefficients at 60N for uniform grid.

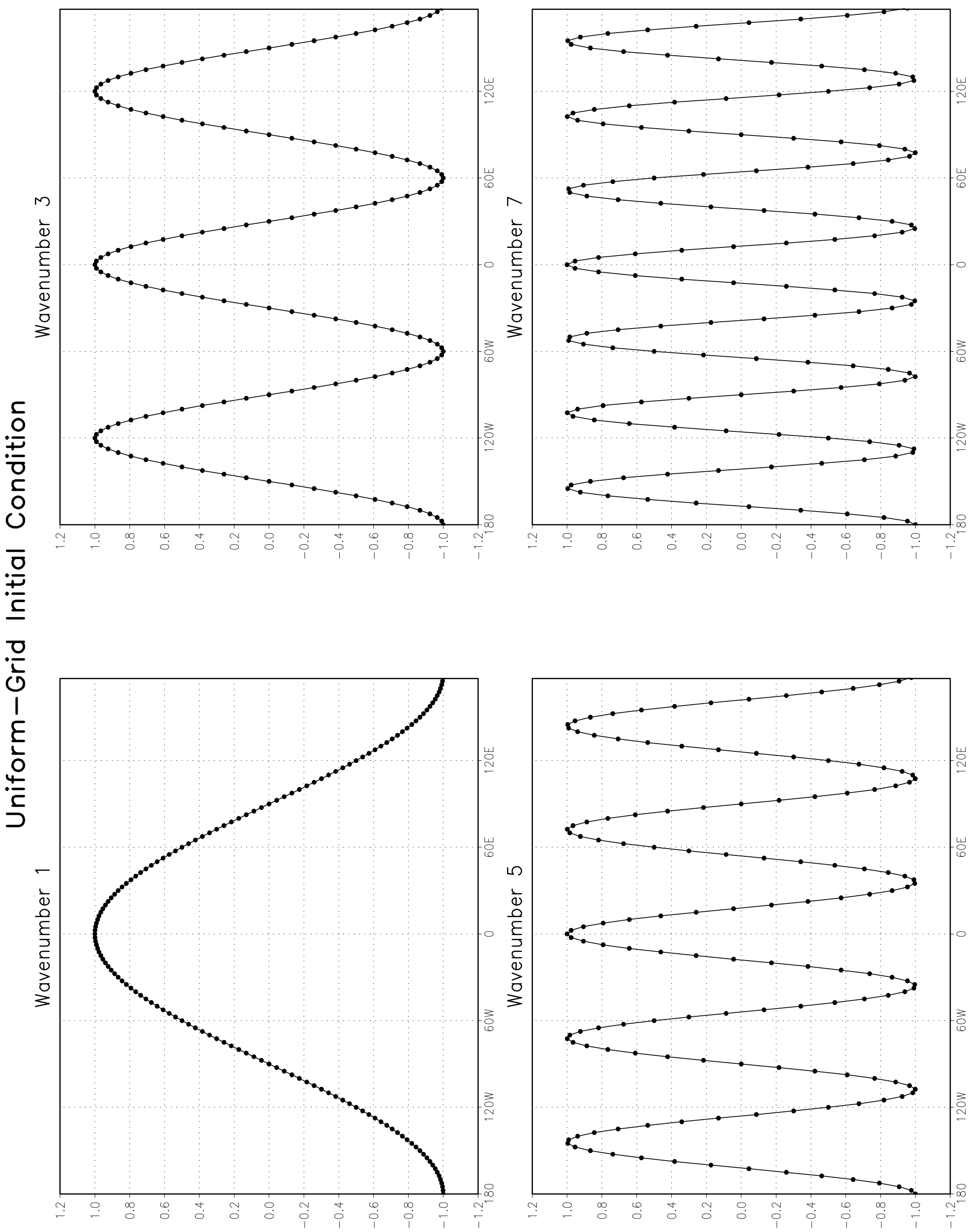

Figure 6: Initial conditions for gravity-wave experiment on a uniform grid.

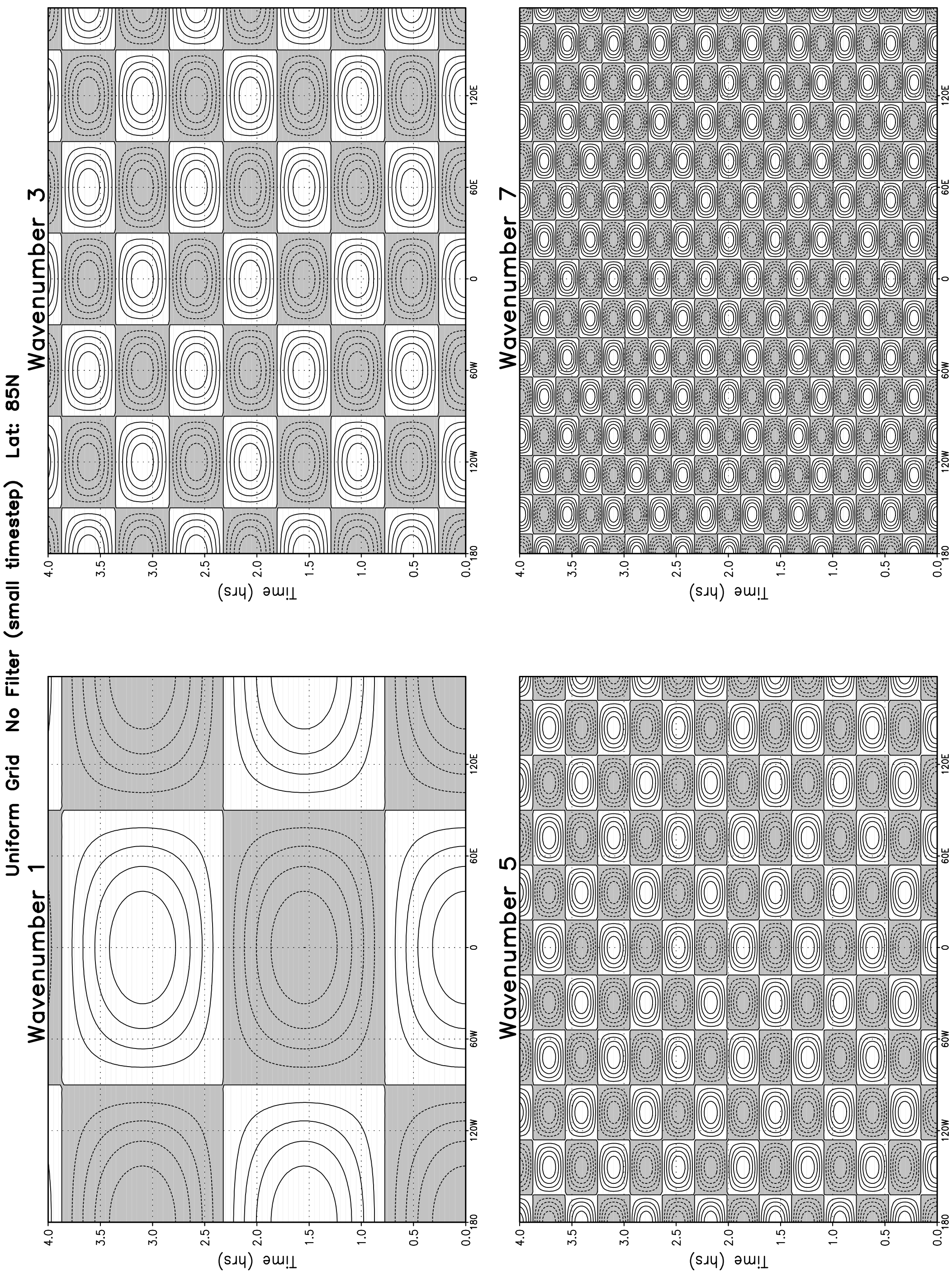

Figure 7: Timeseries of single harmonics on a uniform grid using a linearly stable timestep and no filtering.

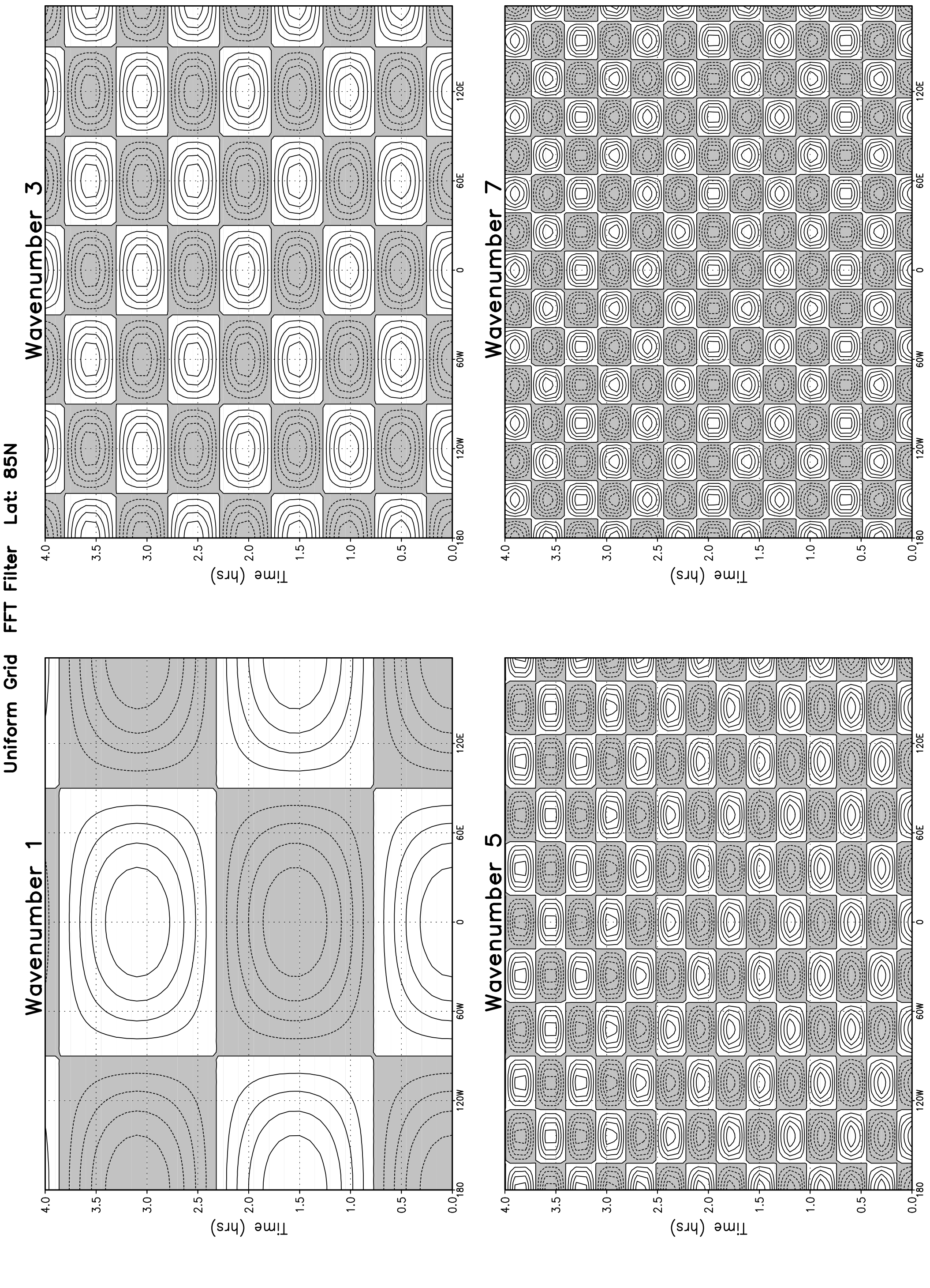

Figure 8: Timeseries of single harmonics on a uniform grid using an unstable timestep with FFT filtering.

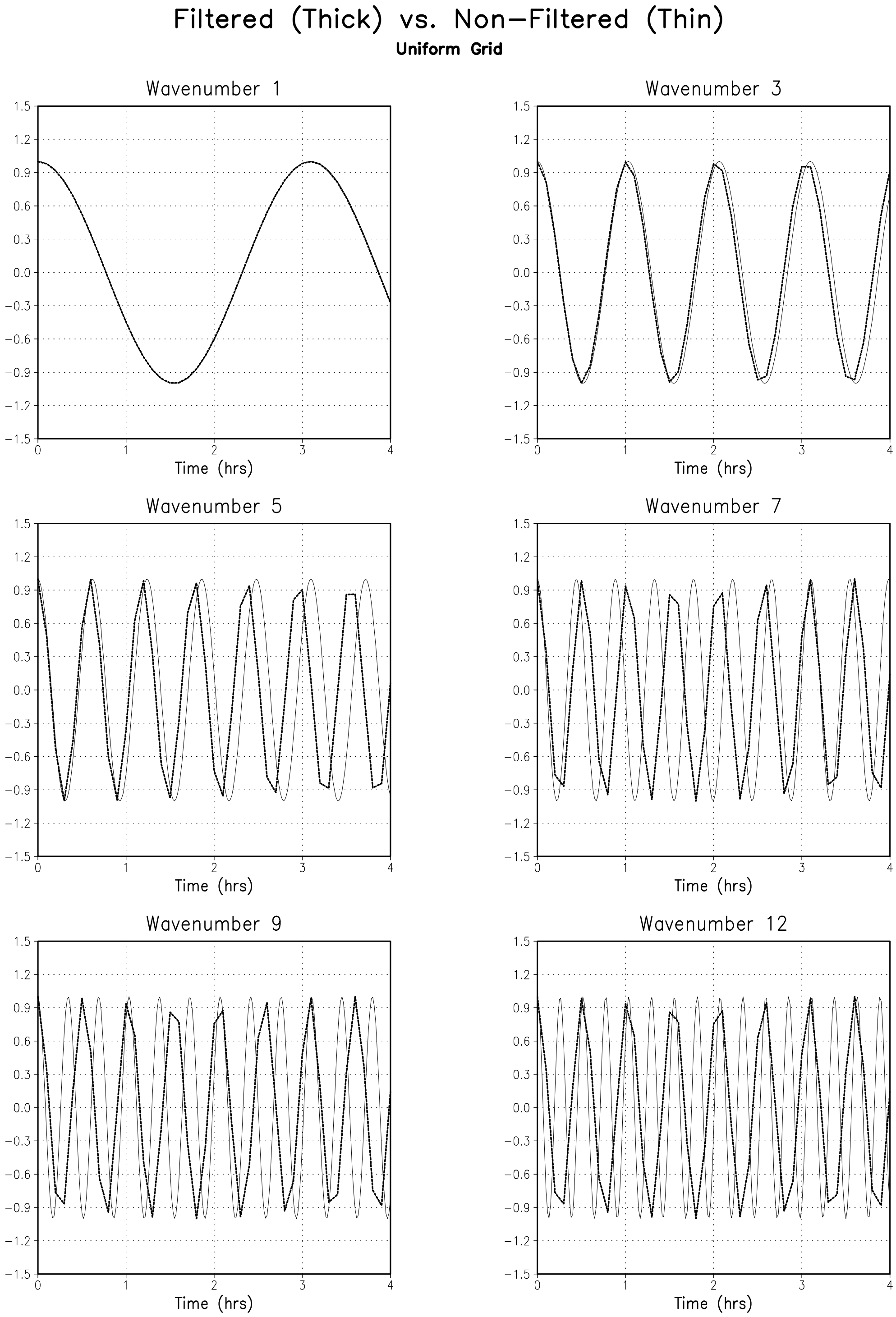

Figure 9: Timeseries at longitude 0 of single harmonics on a uniform grid comparing filtered (thick) and non-filtered (thin) runs.

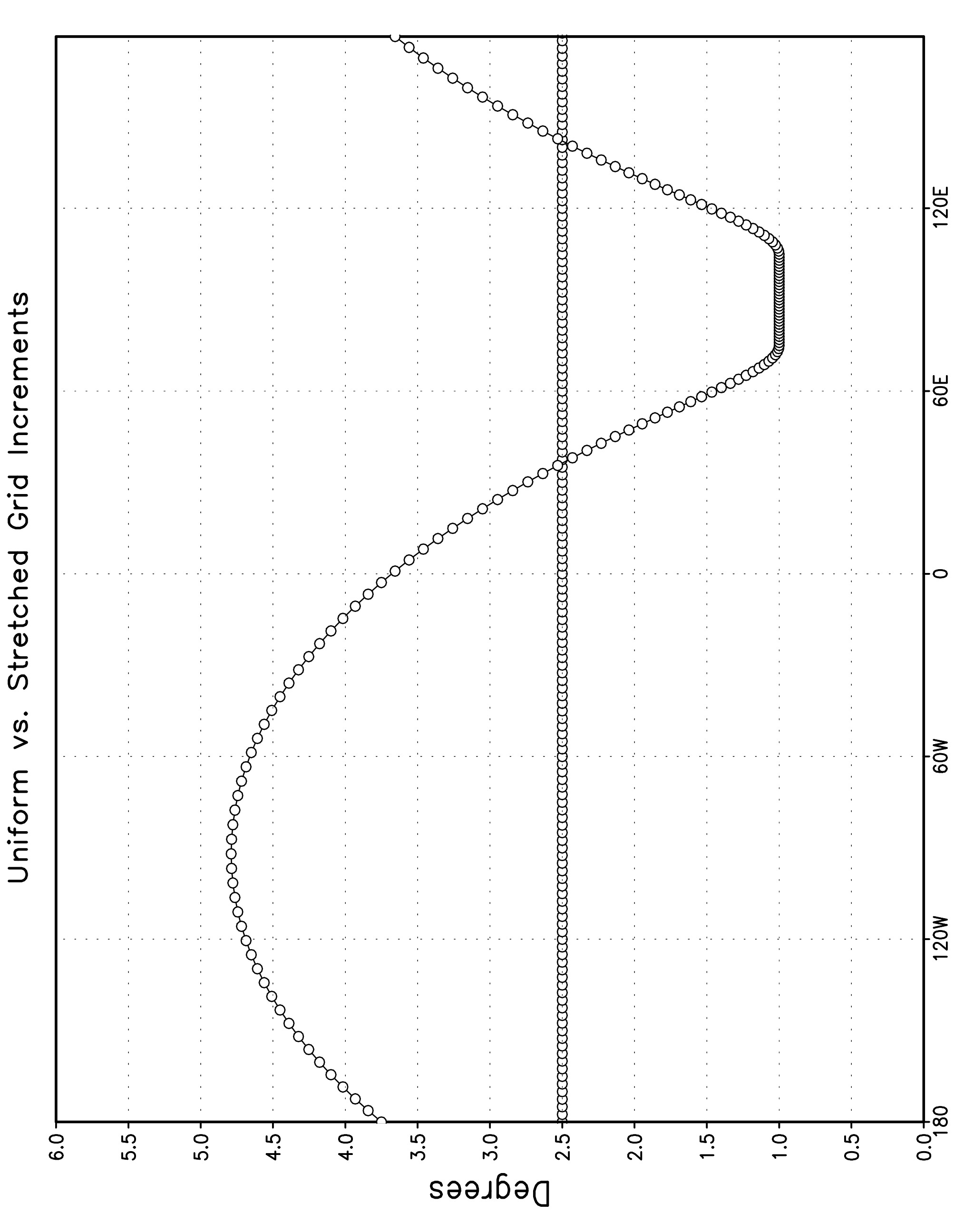

Figure 10: A comparison of the uniform and stretched-grid zonal increments.

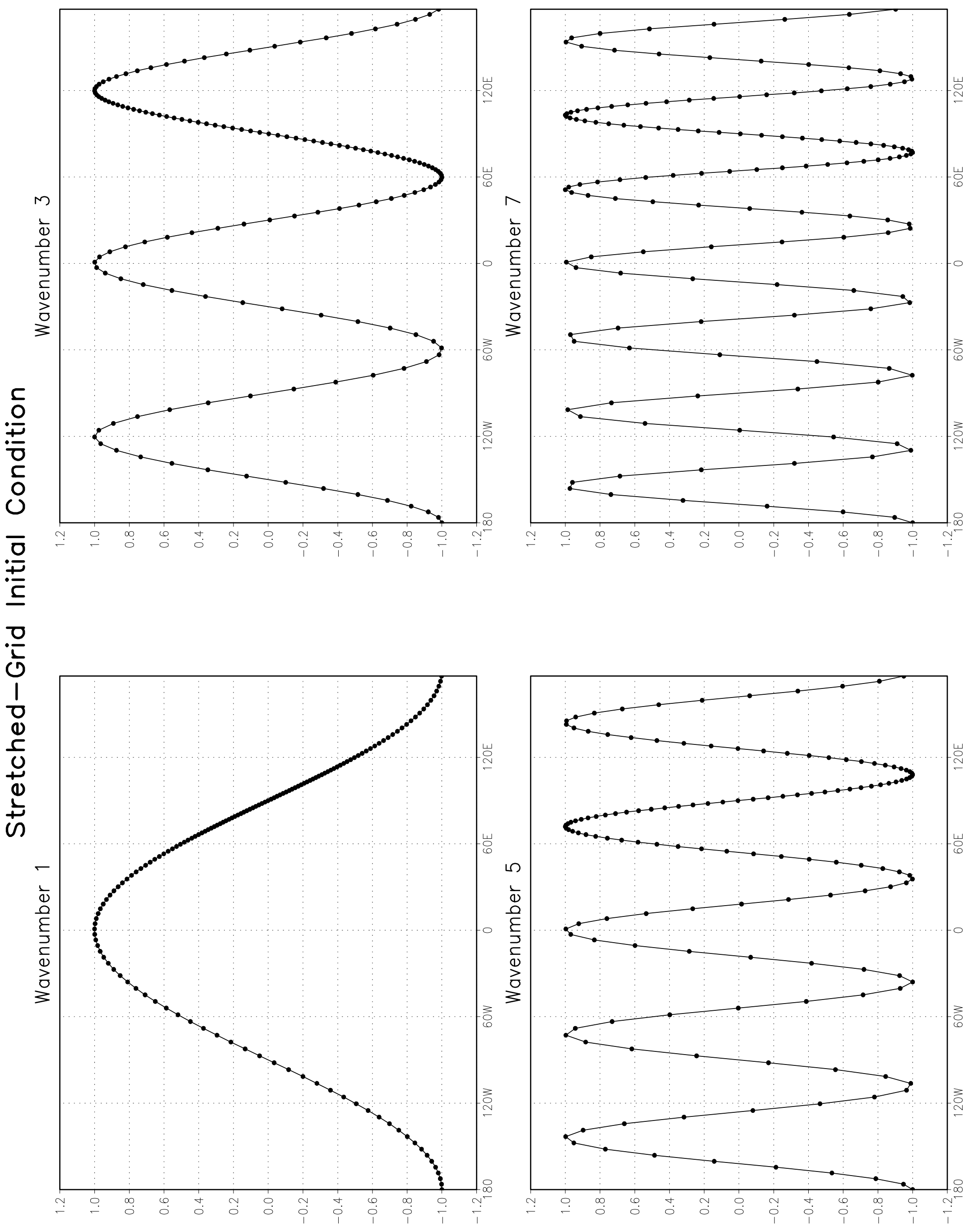

Figure 11: Initial conditions for gravity-wave experiment on a stretched grid.

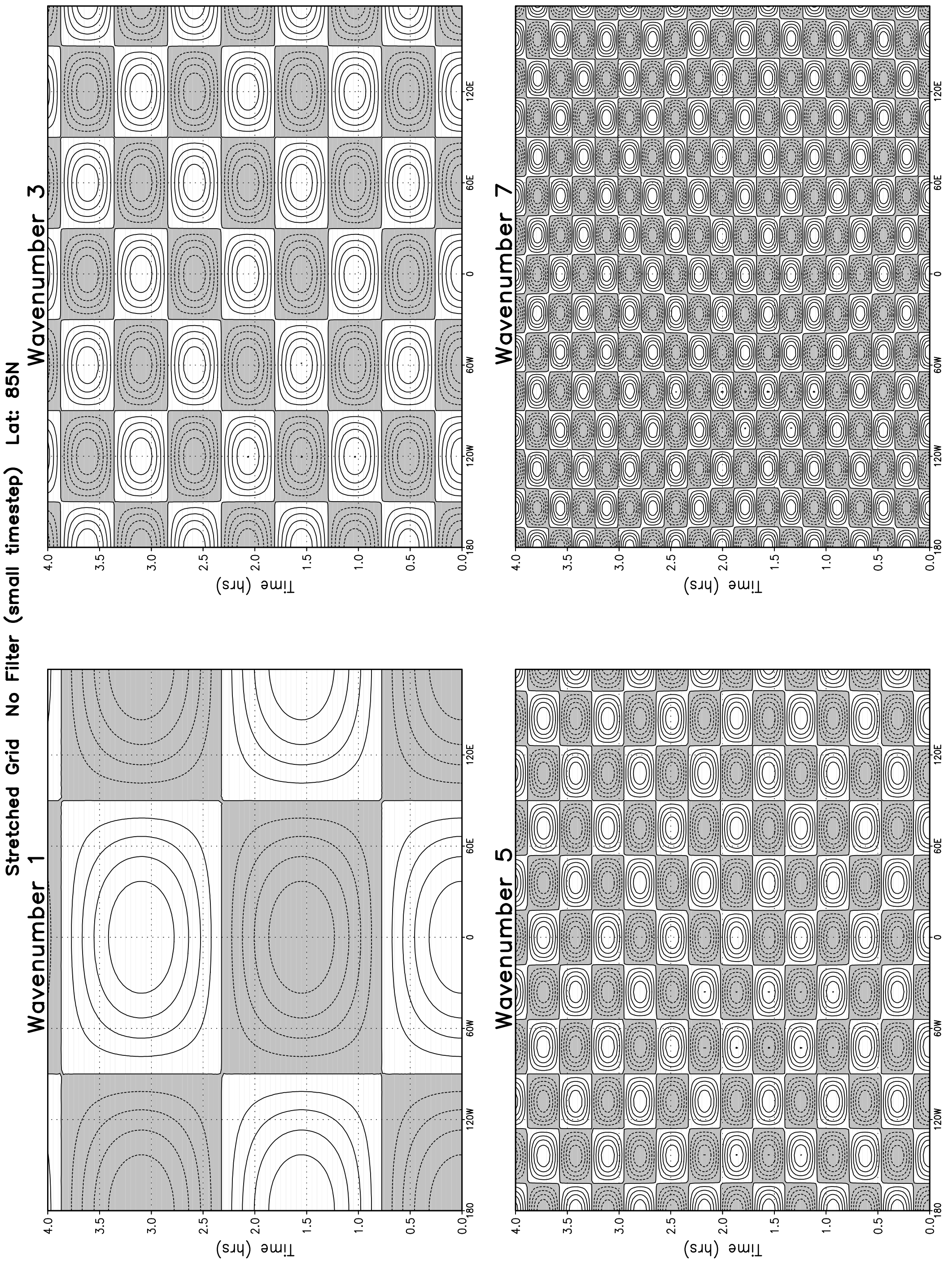

Figure 12: Timeseries of single harmonics on a stretched grid using a linearly stable timestep and no filtering.

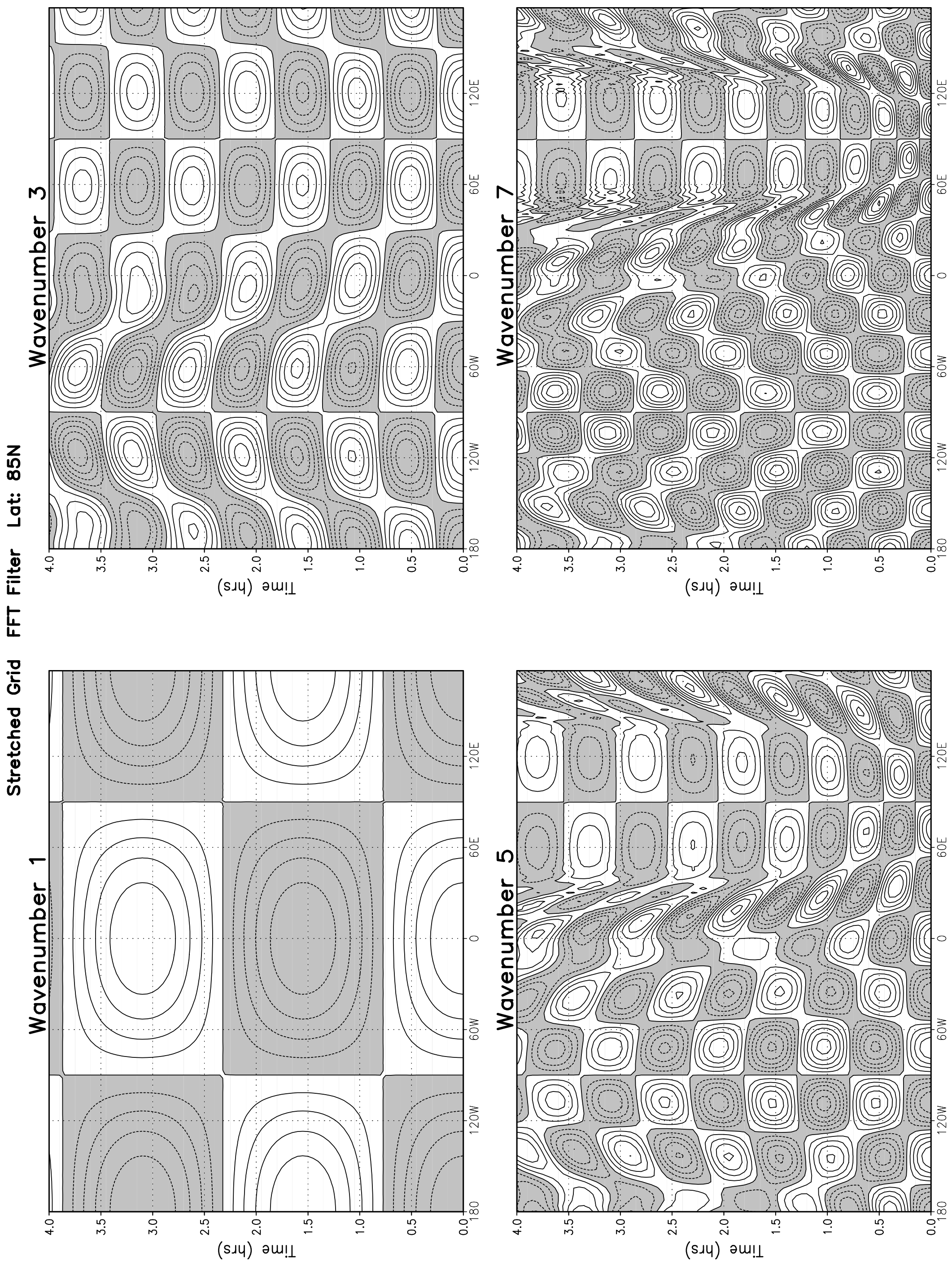

Figure 13: Timeseries of single harmonics on a stretched grid using an unstable timestep with FFT filtering.

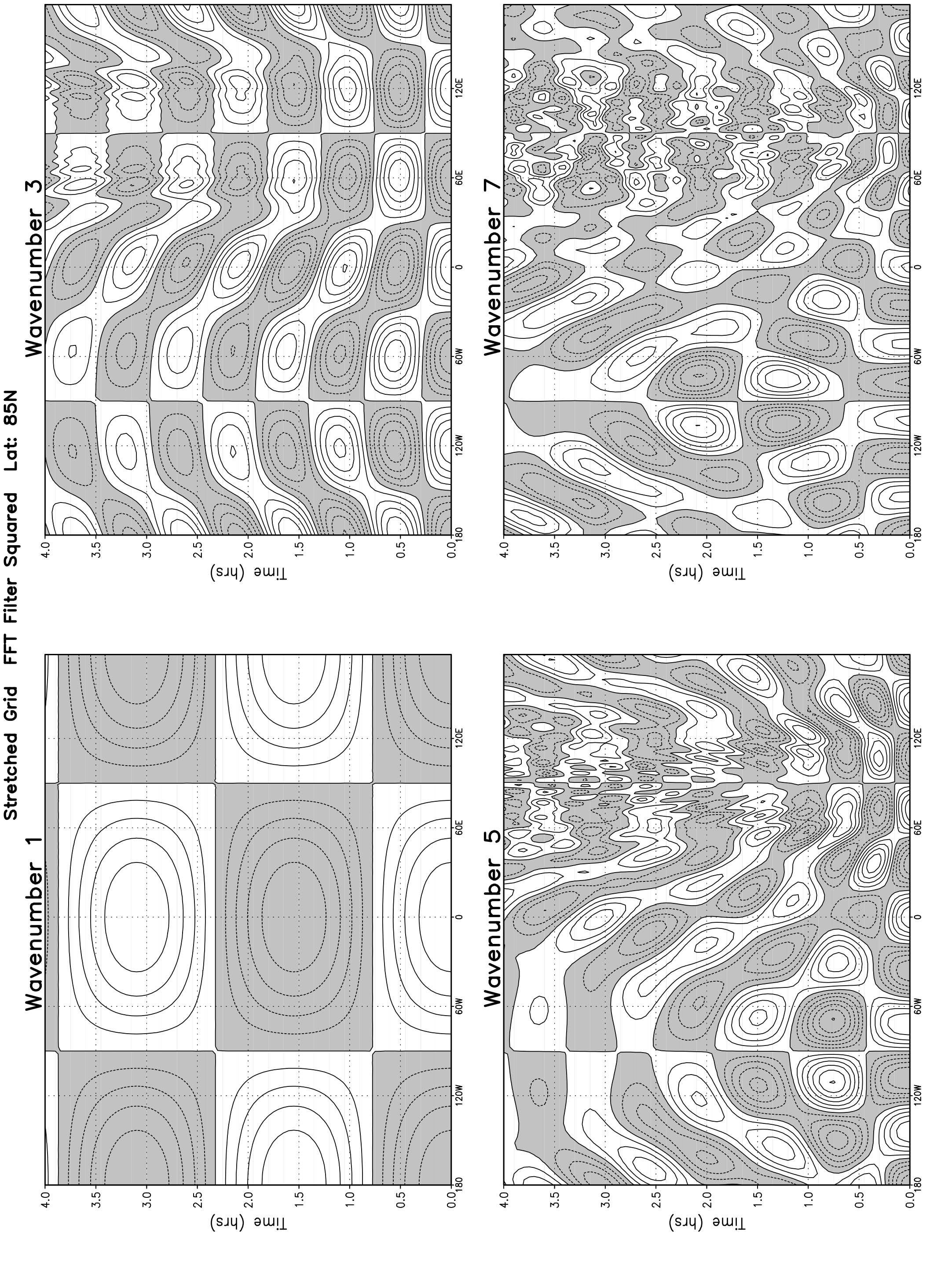

Figure 14: Timeseries of single harmonics on a stretched grid using the FFT filter squared.

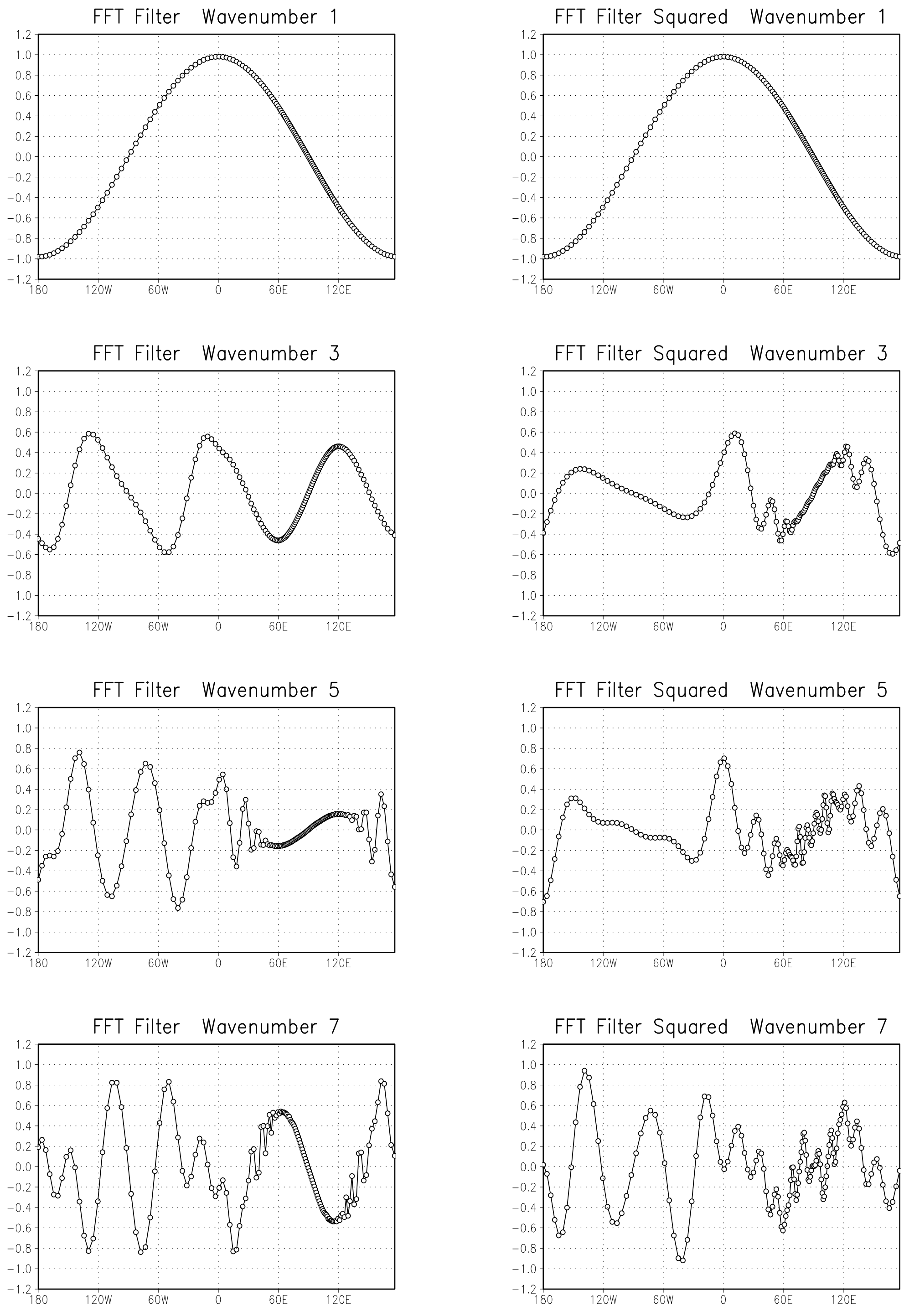

Figure 15: Single harmonics at time = 3 hrs using the standard FFT filter and FFT filter squared on the stretched grid.

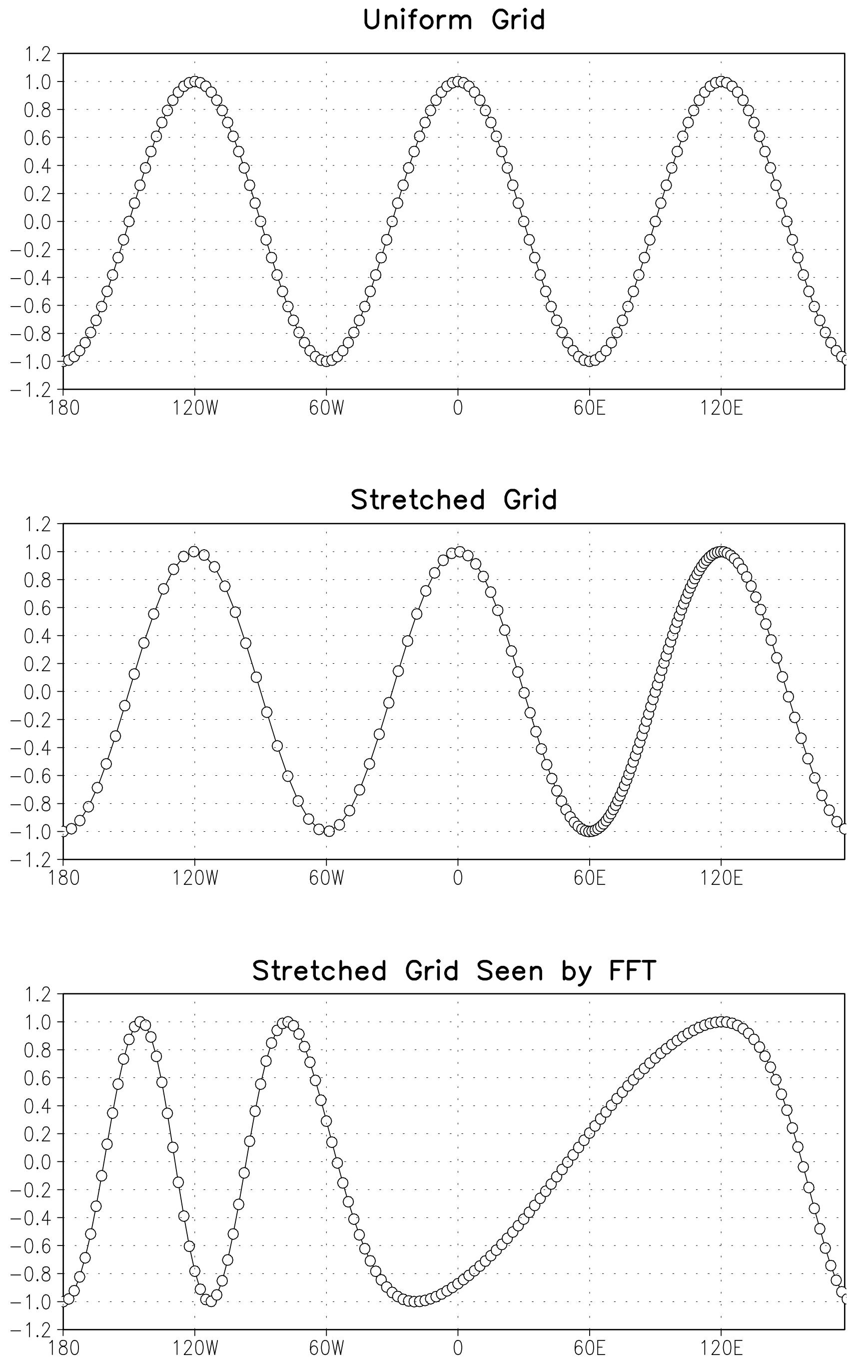

Figure 16: Wavenumber 3 as seen by Uniform Grid, Stretched Grid, and Stretched Grid interpretted as Uniform Grid.

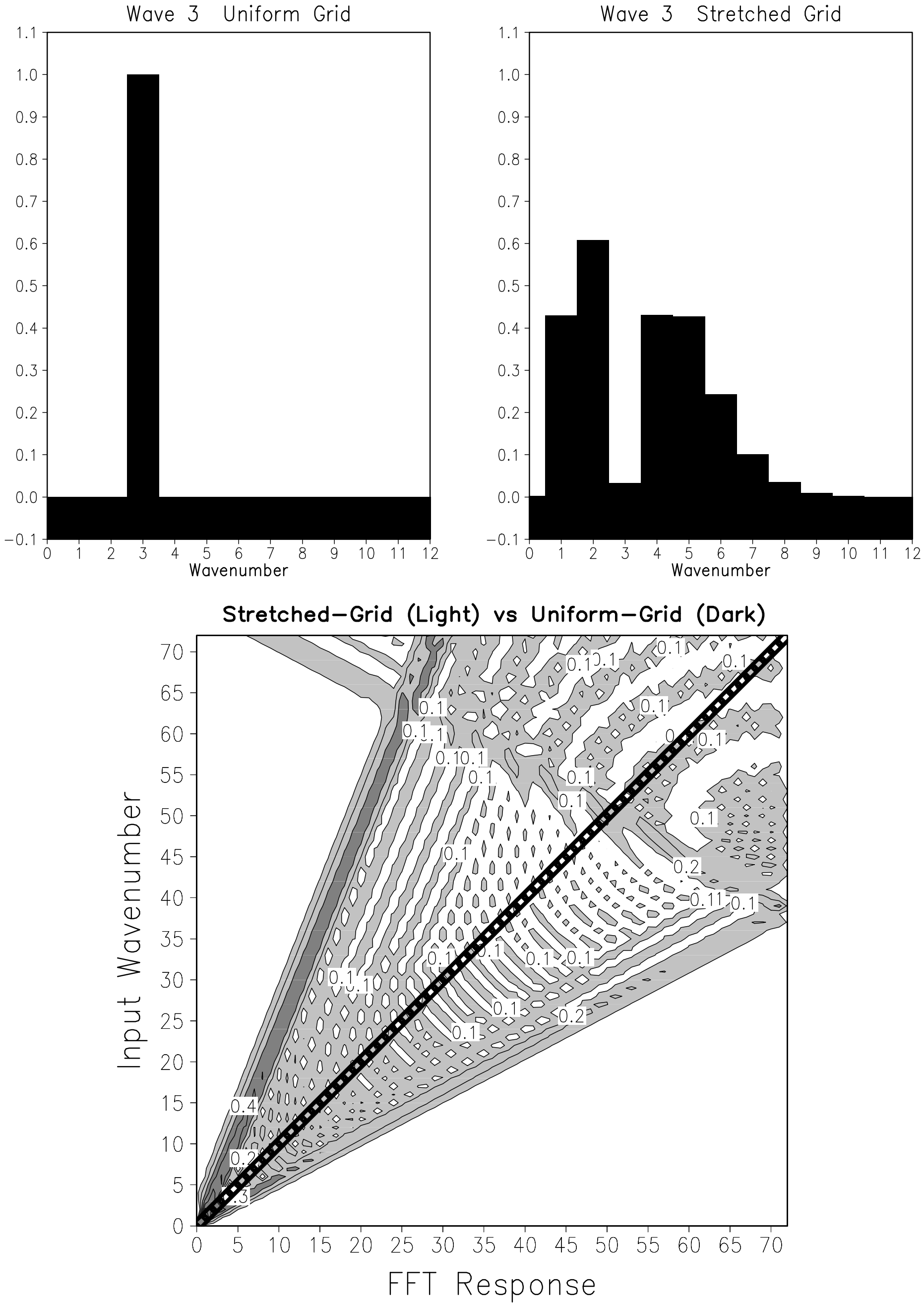

Figure 17: Spectral decomposition of single harmonic waves as interpretted by FFT on the Stretched Grid.

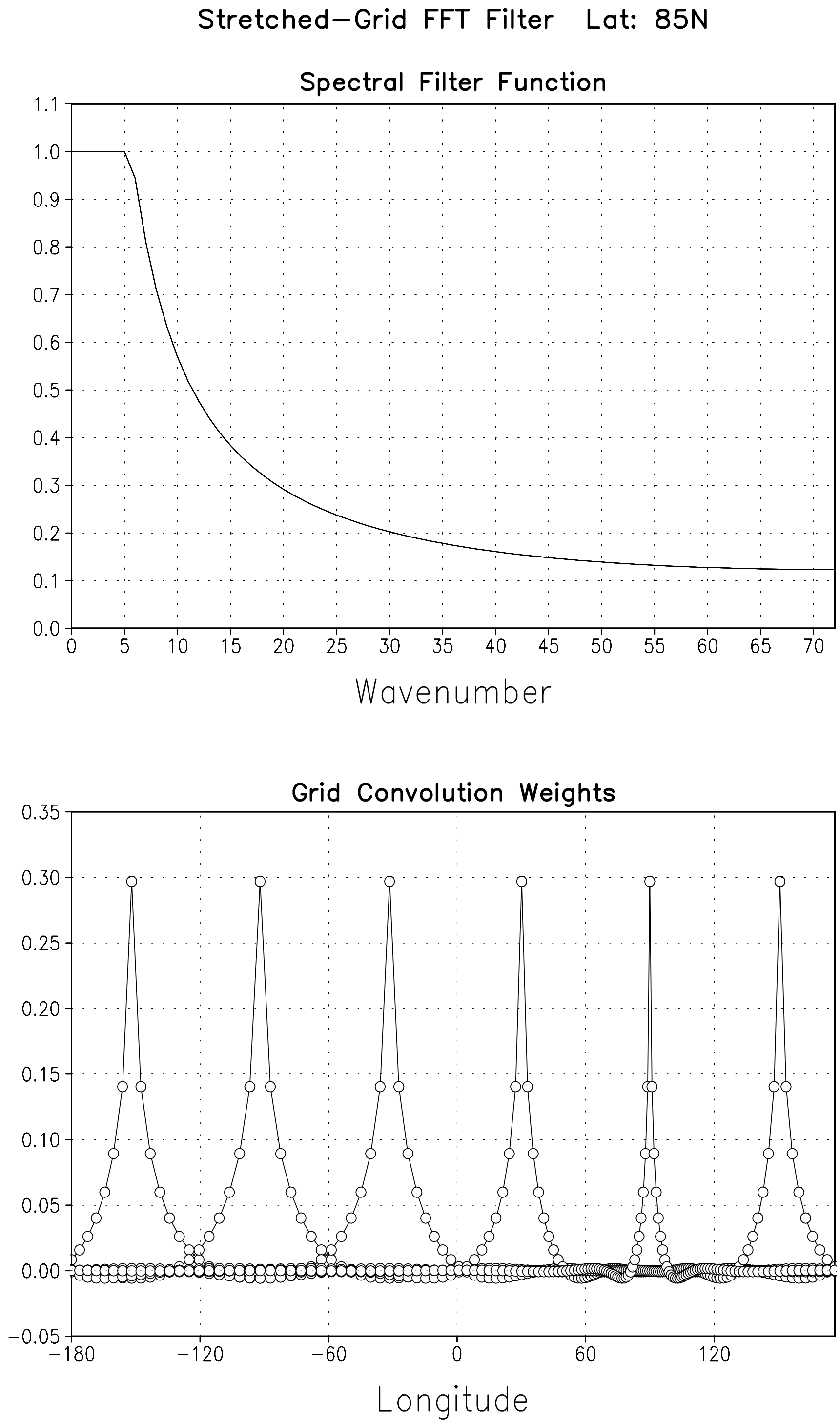

Figure 18: Filter function and grid-space weighting coefficients using standard FFT on a stretched grid.

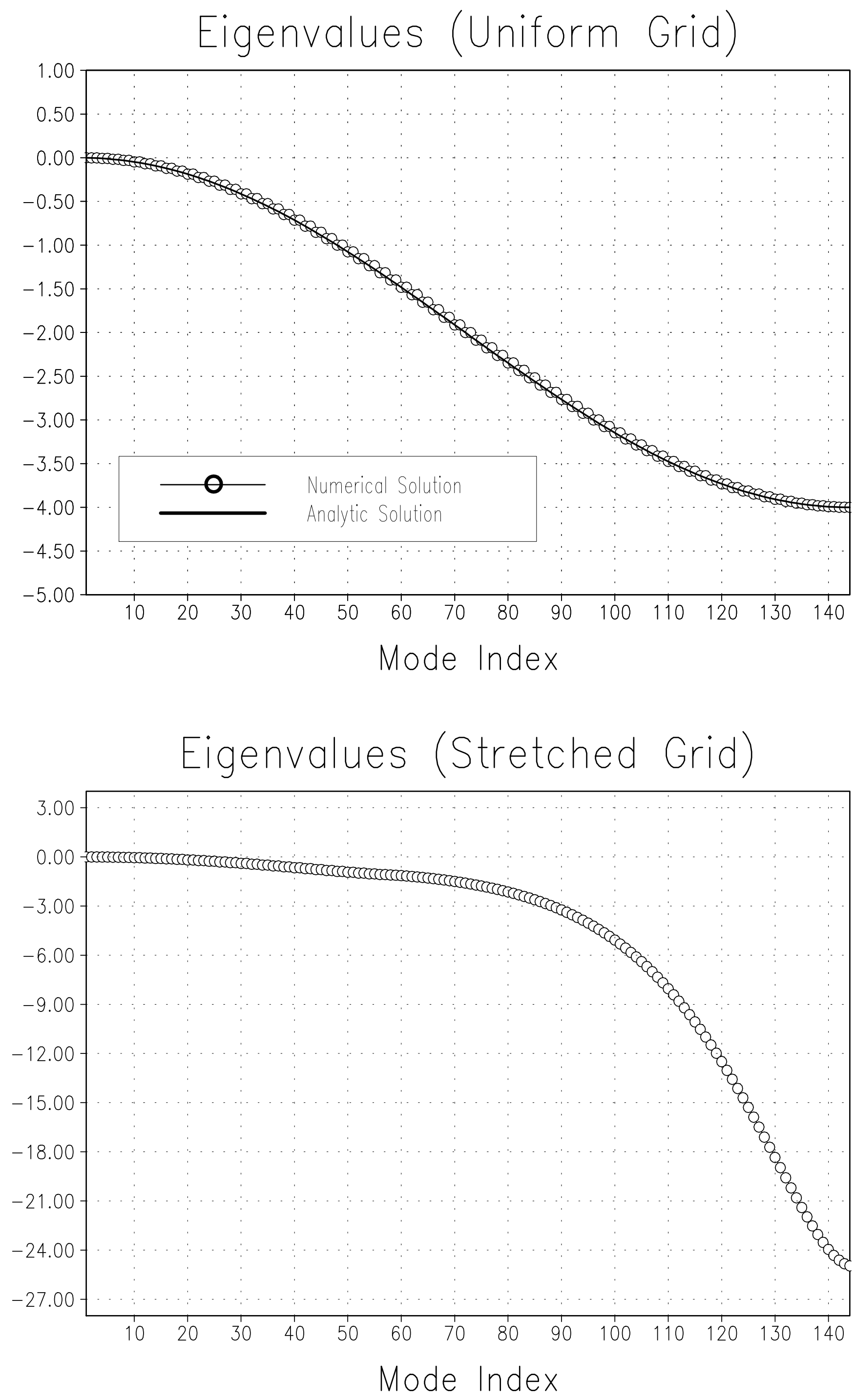

Figure 19: Eigenvalues associated with the uniform and stretched grid.

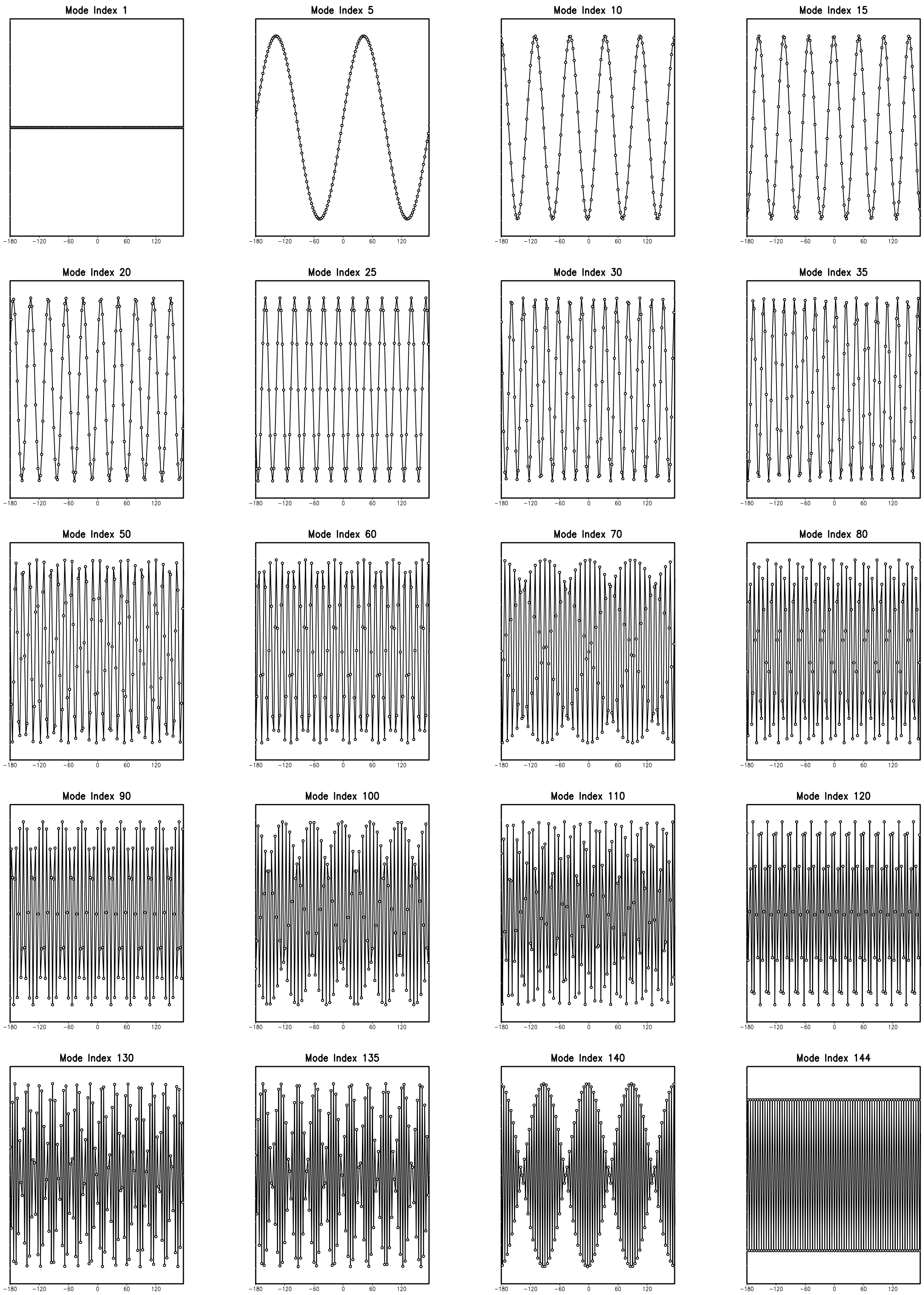

Figure 20: Eigenvectors associated with the uniform grid.

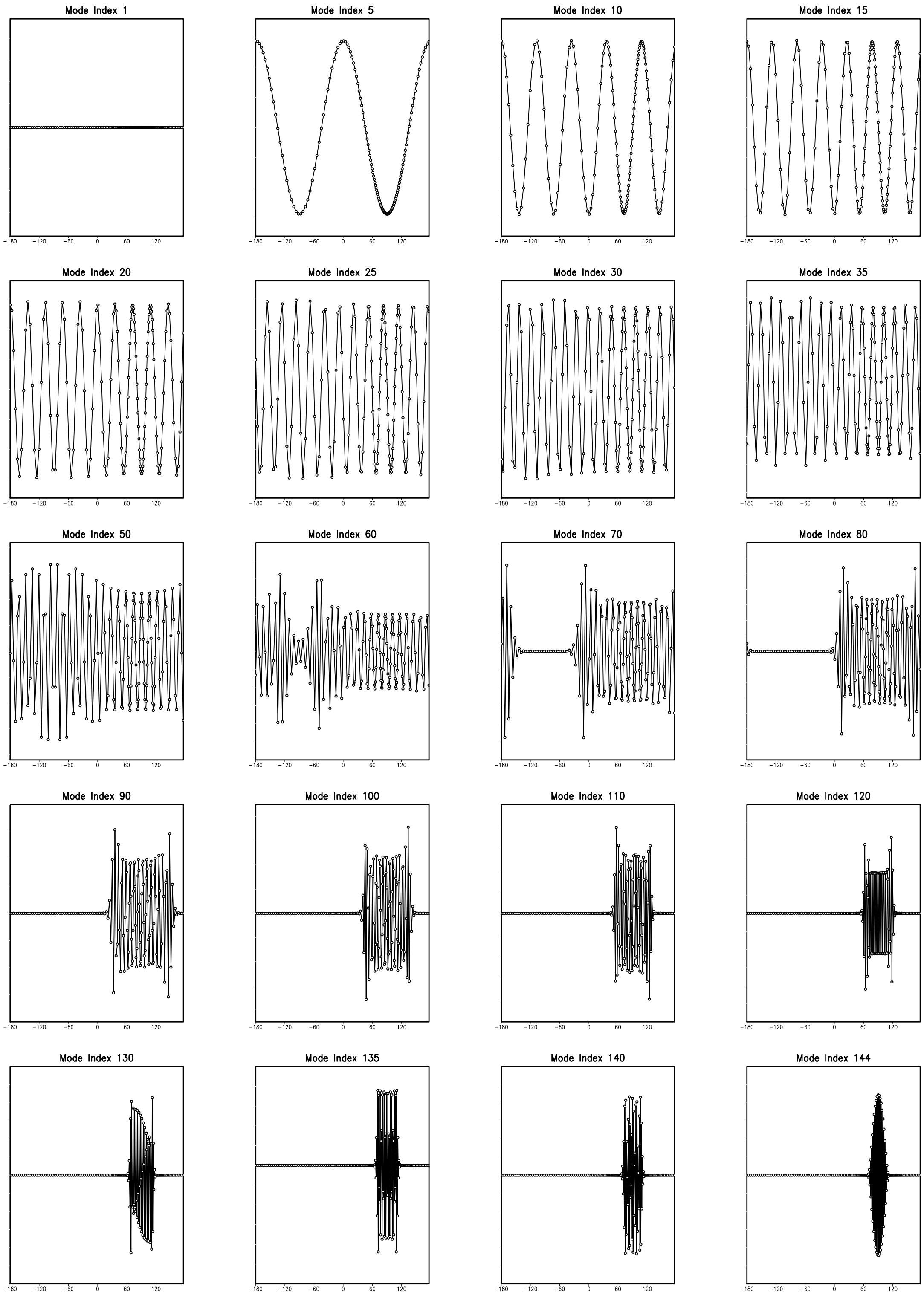

Figure 21: Eigenvectors associated with the stretched grid.

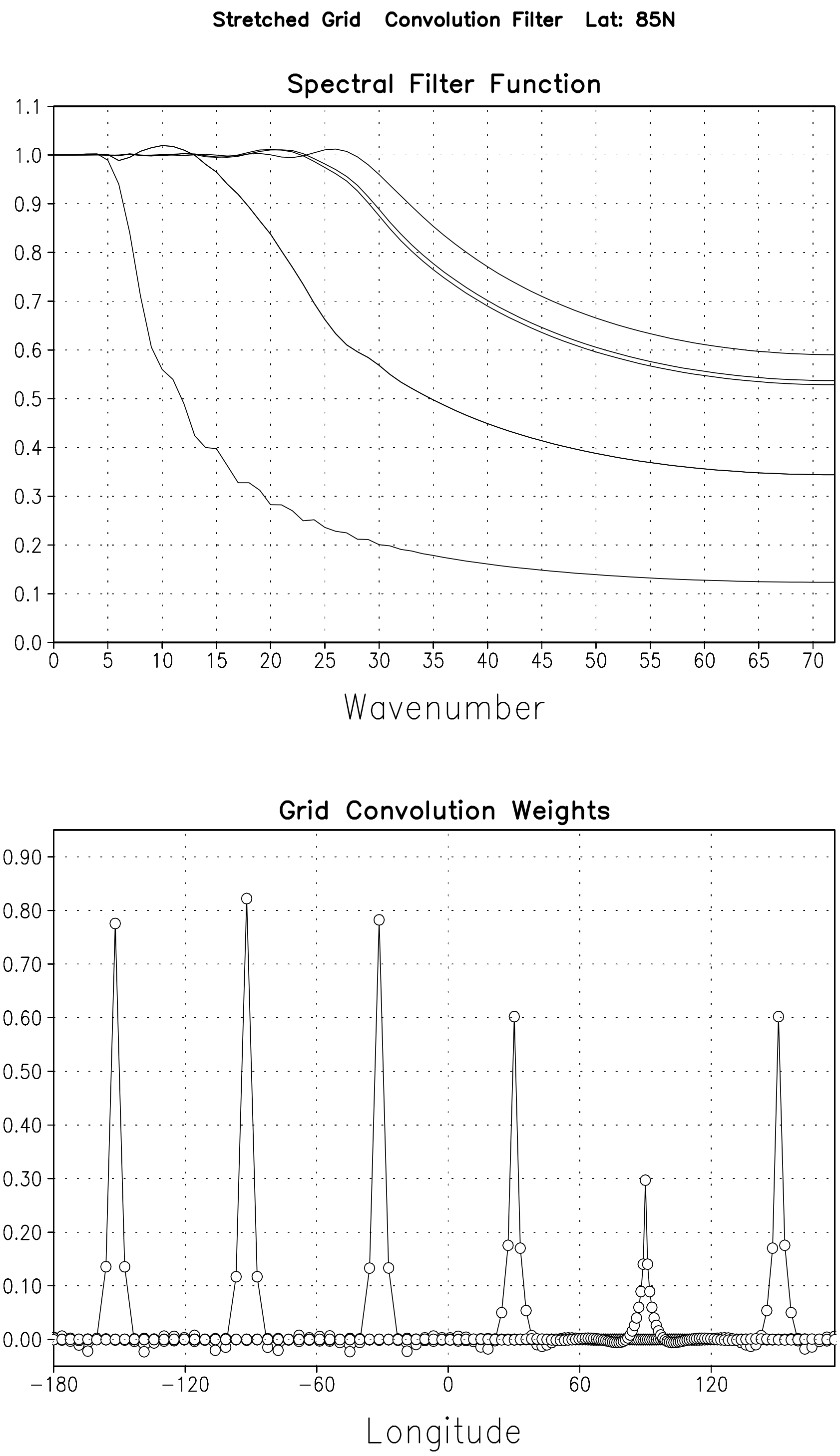

Figure 22: Filter function and grid-space weighting coefficients using the convolution filter on a stretched grid.

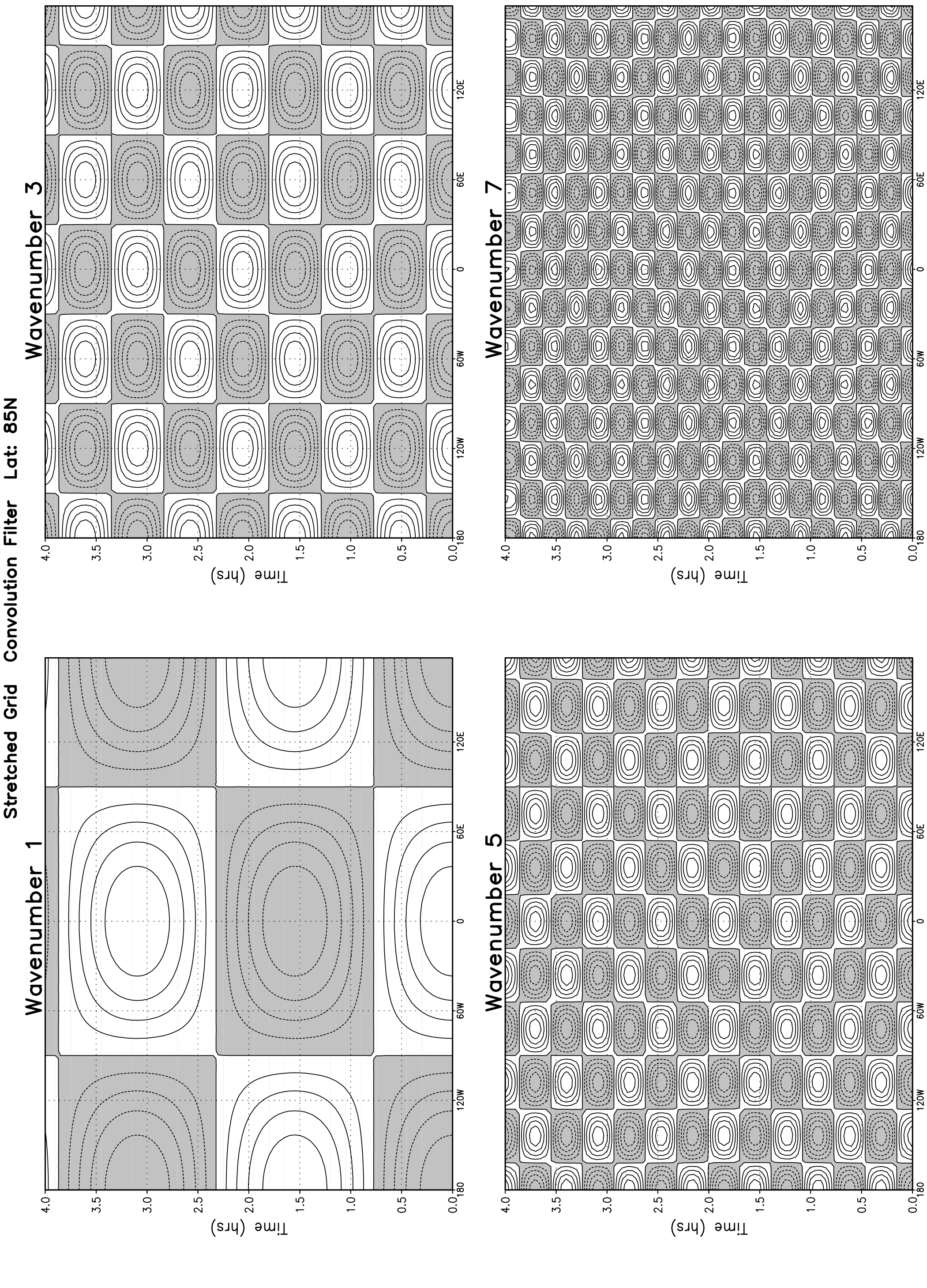

Figure 23: Timeseries of single harmonics on a stretched grid using an unstable timestep with convolution filtering.

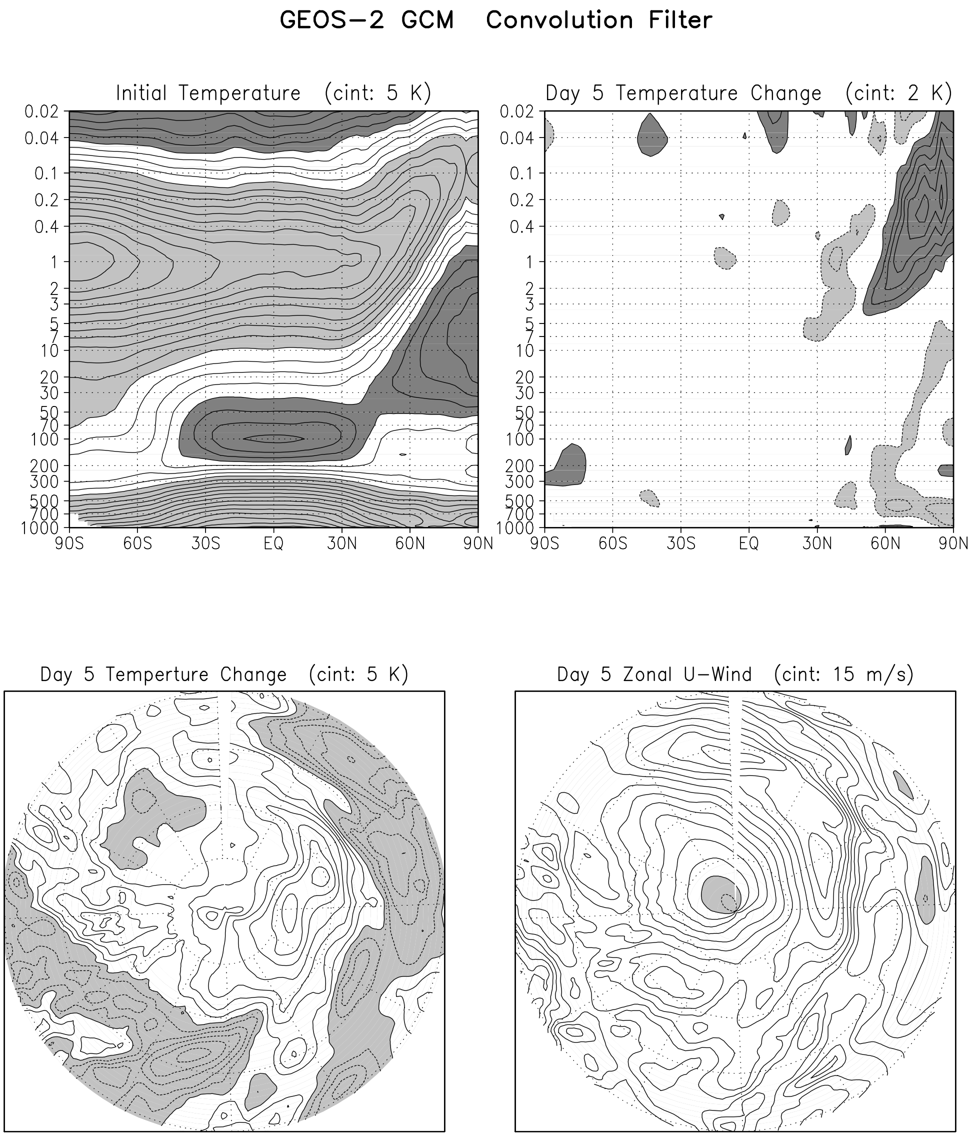

Figure 24: Initial temperature and Day 5 temperature change (top panel), and 0.2 mb temperature change and zonal wind field (bottom panel) using the convolution filter on the stretched grid.

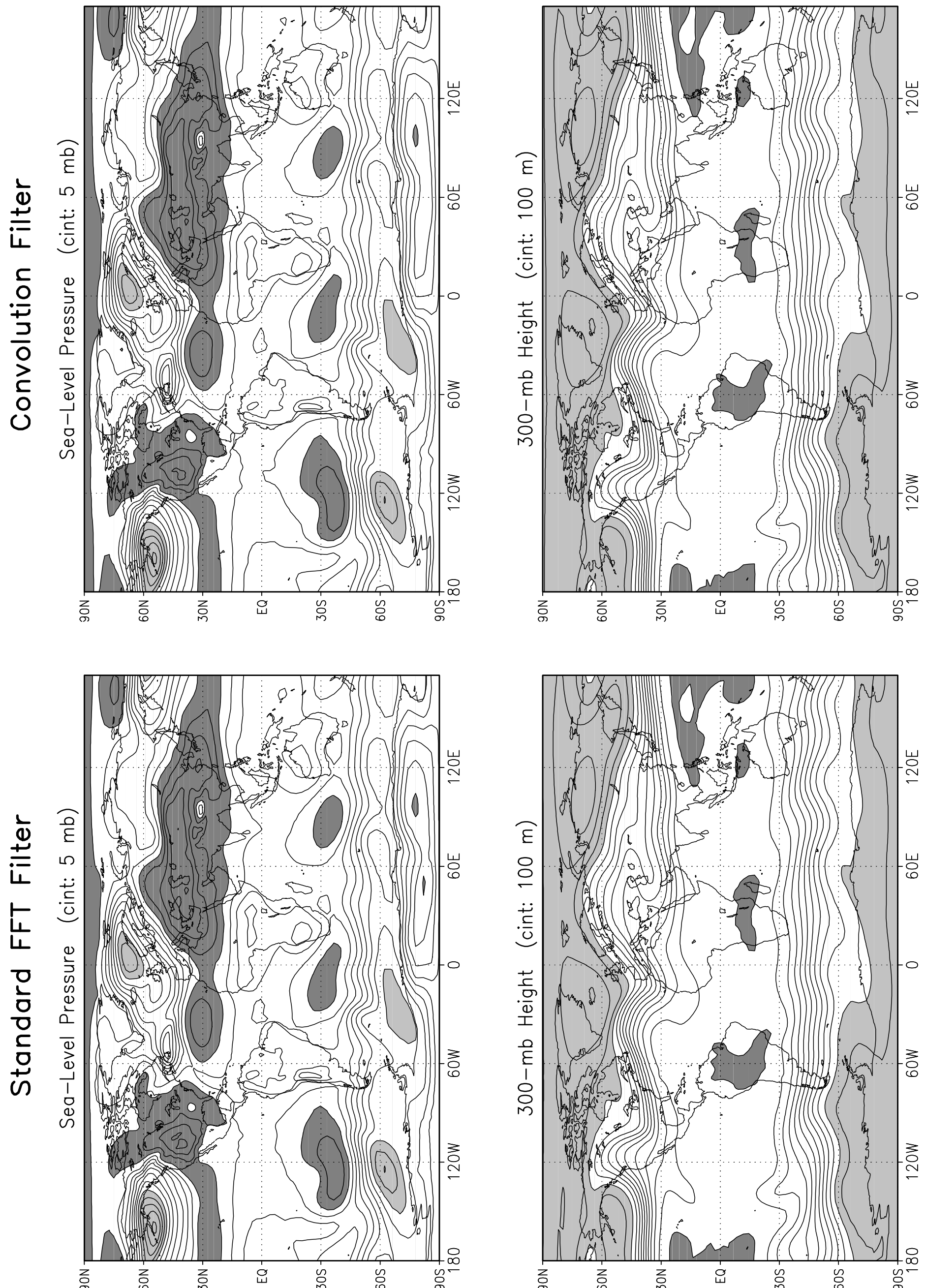

Figure 25: Day 5 sea-level pressure and 300-mb height fields for the standard FFT filter and the convolution filter.

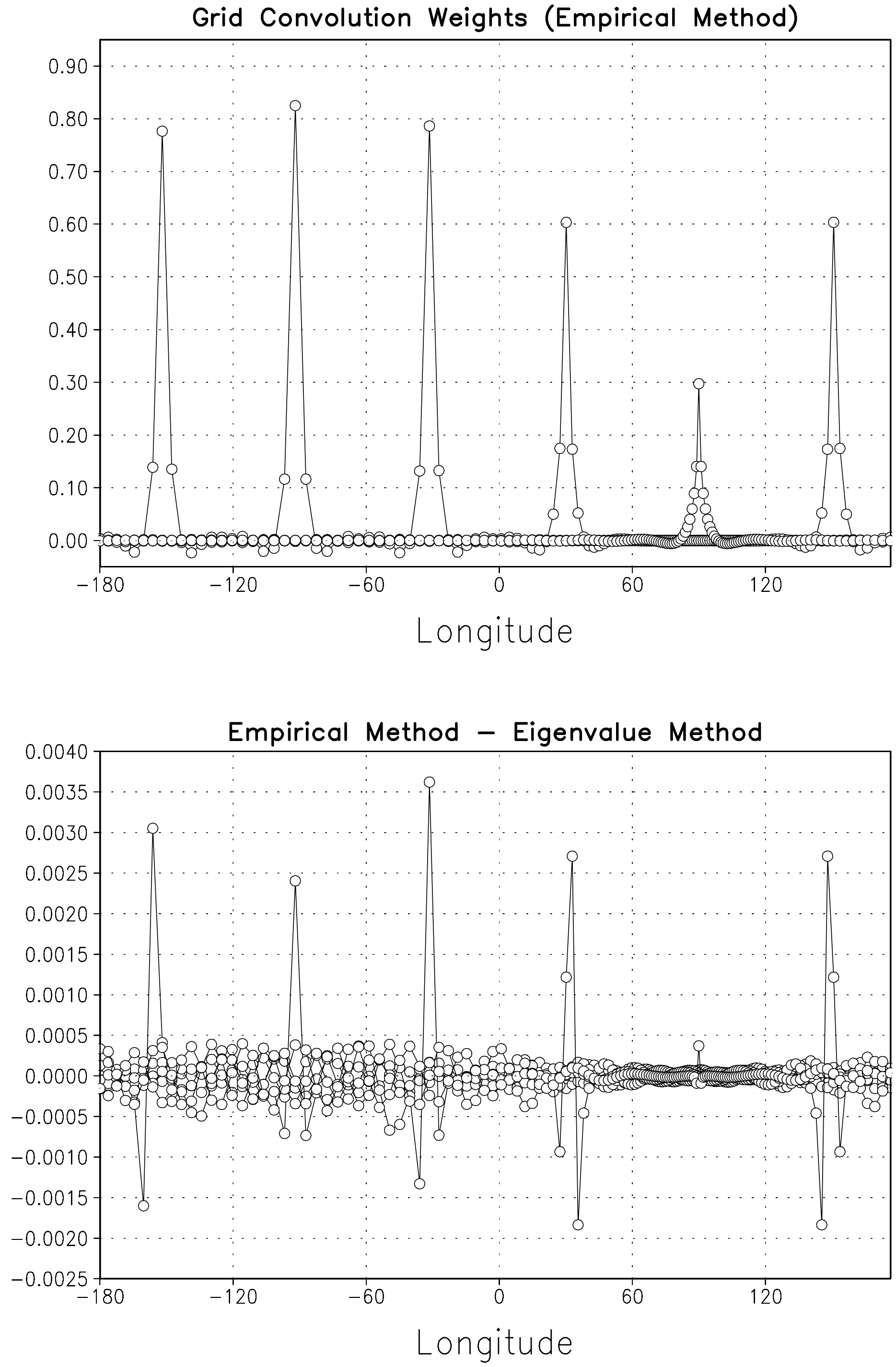

Figure 26: Grid-space weighting coefficients using the empirical method, and compared with the eigenvalue method.

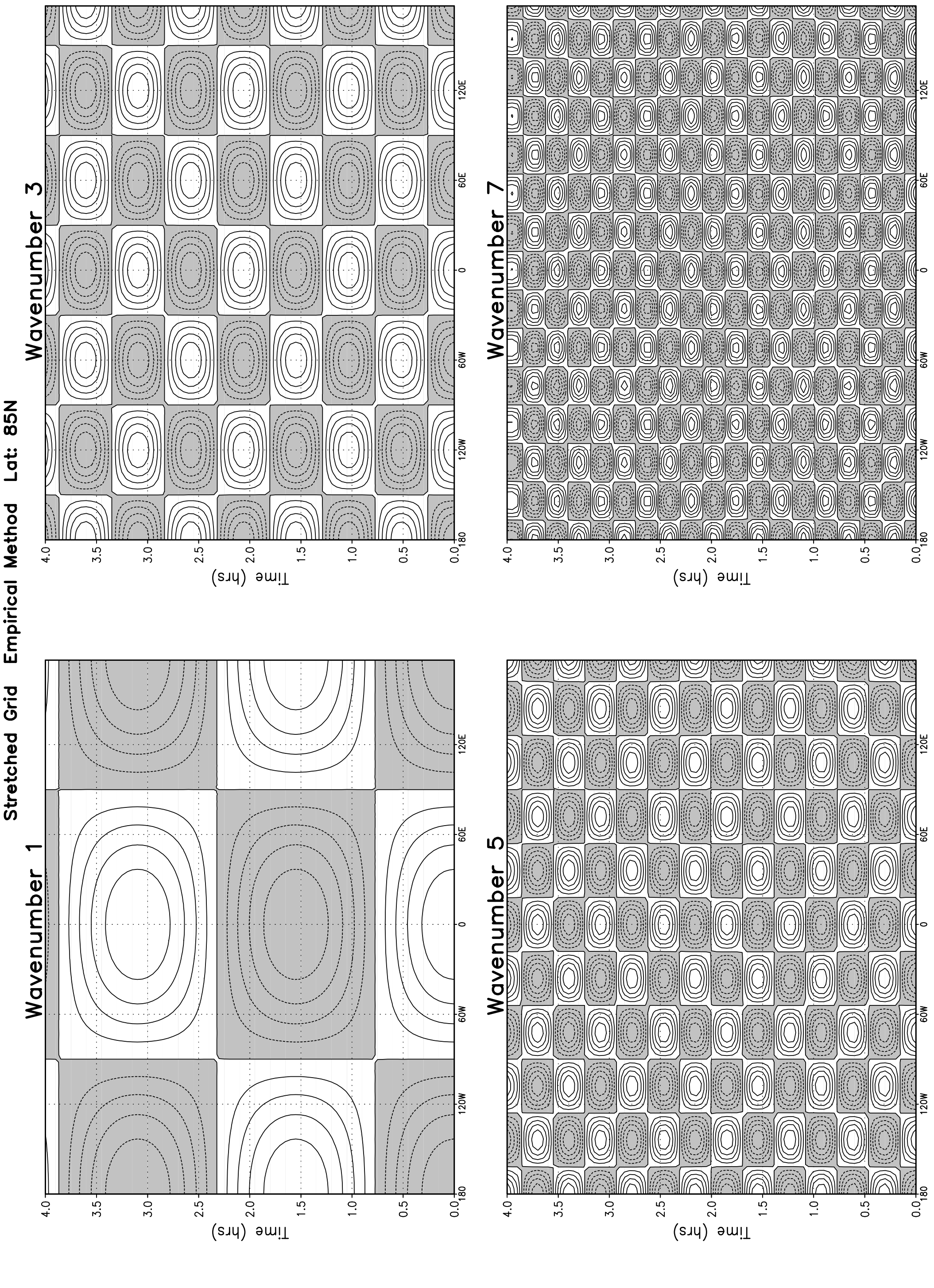

Figure 27: Timeseries of single harmonics on a stretched grid with weights obtained using the empirical method.

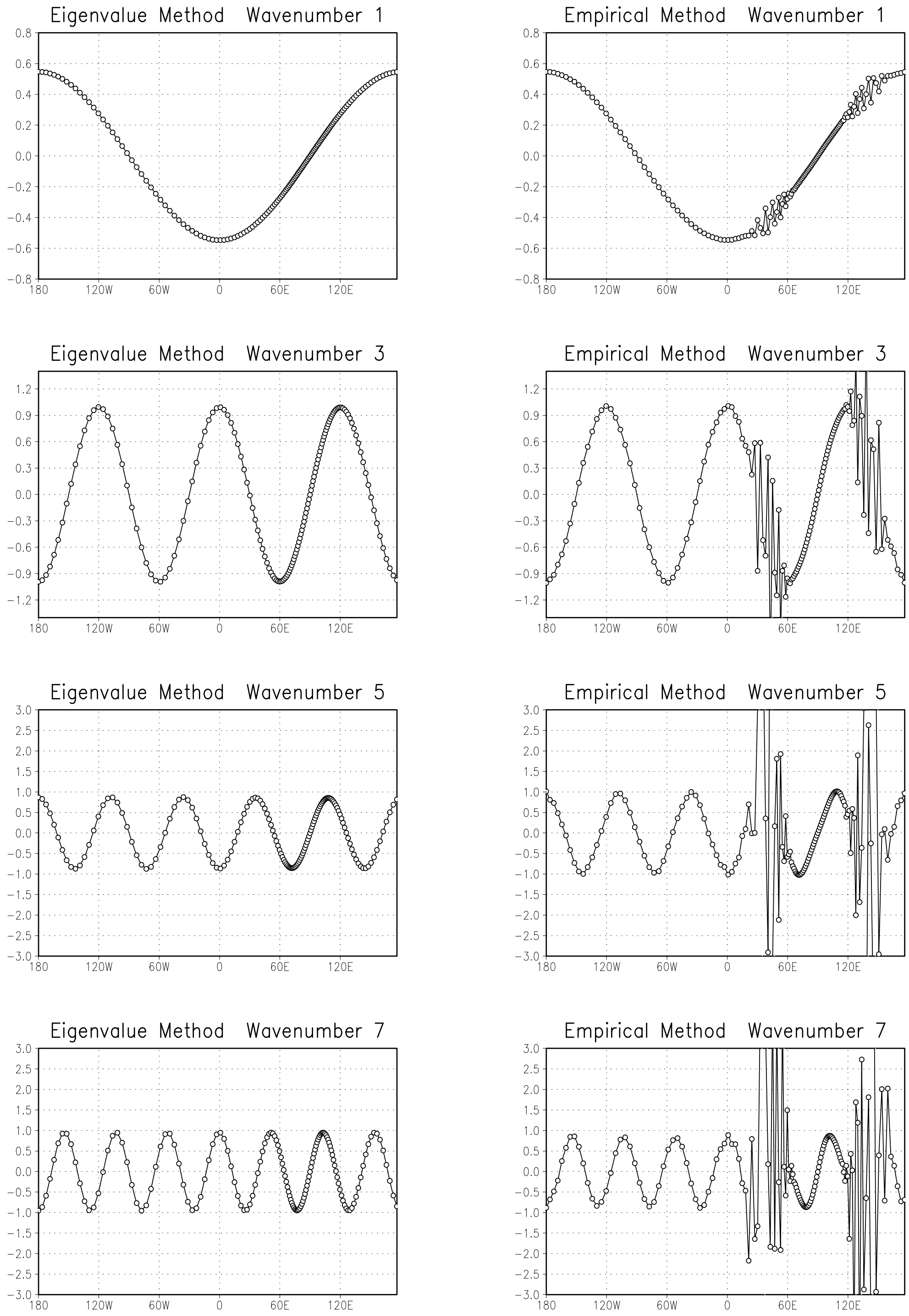

Figure 28: Single harmonics at time = 30 hrs comparing the eigenvalue and empirial methods.

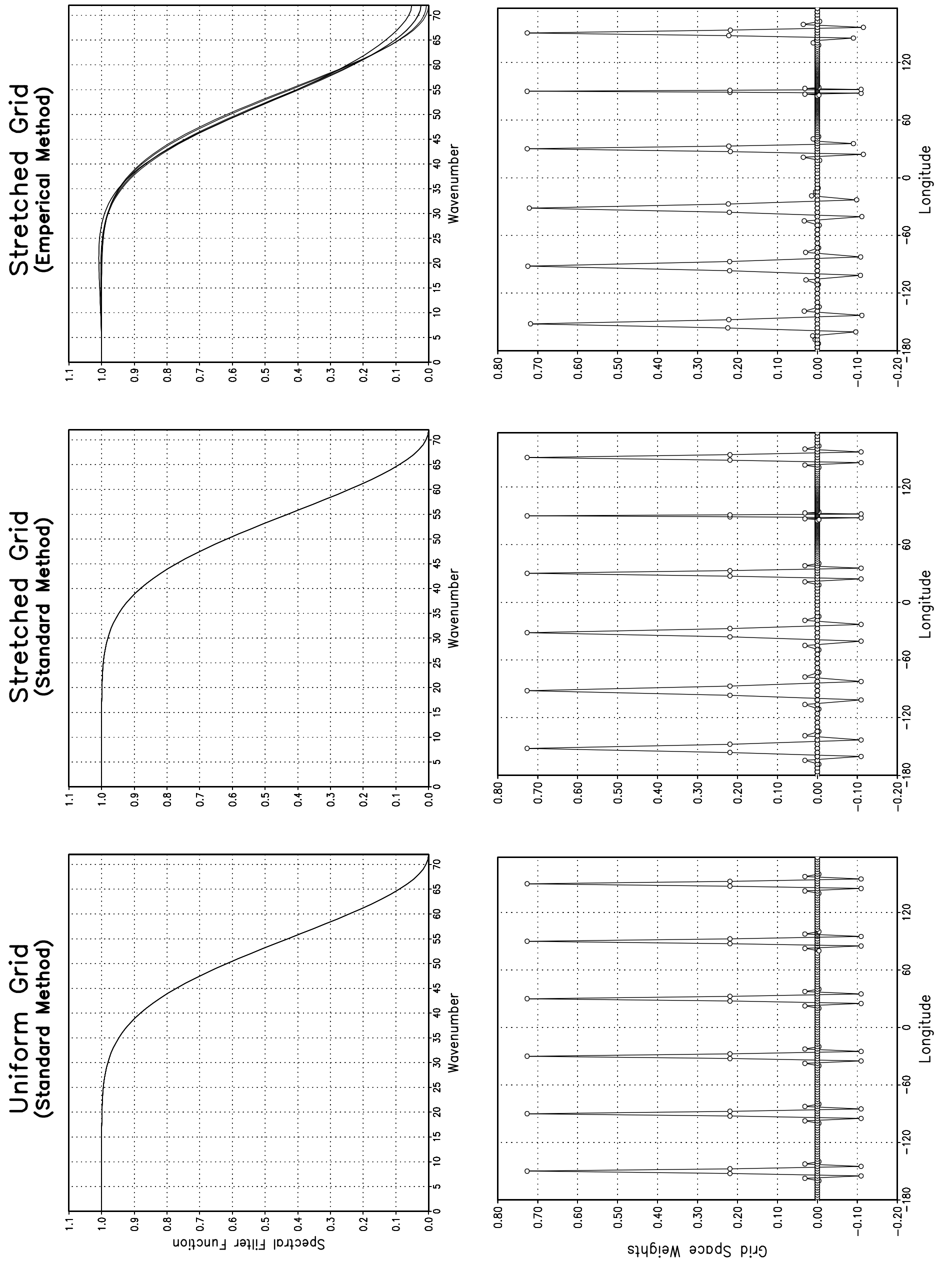

Figure 29: Filter function and grid space weights for an 8th-order Shapiro filter on the uniform and stretched grid.

References

Fox-Rabinovitz, M., G.L. Stenchikov, M.J. Suarez, and L.L. Takacs, 1997: A Finite-Difference GCM Dynamical Core with a Variable-Resolution Stretched Grid. *Mon. Wea. Rev.*, **125**, 2943-2968.

Gates, W. Lawrence, 1992: AMIP: The Atmospheric Model Intercomparison Project. *Bull. Am Met. Soc.*, **73**, 1962-1970

Golub, G. and C. Van Loan, 1989: *Matrix Computations.* Johns Hopkins University Press, Baltimore, MD.

Held., I.M., and M.J. Suarez, 1994: A benchmark calculation for the dry dynamical cores of atmospheric general circulation models. *Bull. Amer. Meteor. Soc.*, **75**, 1825-1830.

Molod, Andrea, H.M. Helfand, and L.L. Takacs, 1996: The Climatology of Parameterized Physical Processes in the GEOS-1 GCM and their Impact on the GEOS-1 Data Assimilation System. *J. Climate*, **9**, 764-785.

Phillips, N.A., 1959: An example of non-linear computational instability. *The Atmosphere and the Sea in Motion*, Rossby Memorial Volume, Rockefeller Institute Press, 501-504.

Rood, R., 1996: Algorithm Theoretical Basis Document for Goddard Earth Observing System Data Assimilation System (GEOS DAS) With a Focus on Version 2. Data Assimilation Office, NASA, Goddard Space Flight Center, Greenbelt, MD.

Schubert, S.D., J. Pfaendtner and R. Rood, 1993: An assimilated data set for Earth Science applications, *Bull. Am Met. Soc.*, **74**, 2331-2342

Schubert, S.D., C.K. Park, C.Y. Wu, W. Higgins, Y. Kondratyeva, A. Molod, L. Takacs, M. Seablom, and R. Rood, 1995: A Multiyear Assimilation with the GEOS-1 System: Overview and Results, NASA Technical Memorandum 104606 Volume 6, NASA, Goddard Space Flight Center, Greenbelt, MD.

Schubert, S.D., and R. Rood, 1995: Proceedings of the Workshop on the GEOS-1 Five-Year Assimilation, NASA Technical Memorandum 104606 Volume 7, NASA, Goddard Space Flight Center, Greenbelt, MD.

Shapiro, R., 1970: Smoothing, filtering and boundary effects. *Rev. Geophys. Space Phys.*, **8**, 359-387.

Suarez, M. J., and L. L. Takacs, 1995: Documentation of the Aries/GEOS Dynamical Core Version 2, NASA Technical Memorandum 104606 Volume 5, NASA, Goddard Space Flight Center, Greenbelt, MD.

Takacs, L. L. , A. Molod, and T. Wang, 1994: Documentation of the Goddard Earth Observing System (GEOS) General Circulation Model-Version 1. NASA Technical Memorandum 104606 Volume 1, Goddard Space Flight Center, Greenbelt, MD 20771.

Takacs, L.L., and M.J. Suarez, 1996: Dynamical aspects of climate simulations Using the GEOS General Circulation Model, NASA Technical Memorandum 104606 Volume 10, NASA, Goddard Space Flight Center, Greenbelt, MD 20771.